https://ntrs.nasa.gov/search.jsp?R=19720016342 2018-07-26T10:13:42+00:00Z

N72-23997

NASA CR-112053

EXPERIMENTAL INVESTIGATION OF HYPERSONIC BUZZ ON A HIGH CROSS-RANGE SHUTTLE CONFIGURATION

By Robert L. Goldman and Henry J. Obremski

May 1972

CASE FILE COPY

RIAS TECHNICAL REPORT 72-05c

Prepared under Contract No. NAS1-10726 by
Research Institute for Advanced Studies
(RIAS)
1450 South Rolling Road
Baltimore, Maryland

for

NATIONAL AERONAUTICS AND SPACE ADMINISTRATION
Langley Research Center

EXPERIMENTAL INVESTIGATION OF HYPERSONIC BUZZ ON A HIGH CROSS-RANGE SHUTTLE CONFIGURATION

By Robert L. Goldman and Henry J. Obremski

SUMMARY

A wind tunnel investigation has been conducted to determine the nature of an unsteady hypersonic flow phenomenon, often referred to as hypersonic buzz, on a 1:100 scale model representative of a high cross-range shuttle configuration. The tests, conducted in helium at a nominal Mach number of 17.5, were specifically directed at obtaining a better understanding of the character of the hypersonic flow field in the vicinity of a deflected control surface. Power spectral densities and root mean squared values of surface pressure fluctuations are presented along with observations made from high speed motion pictures, schlieren and oil flow photographs. Flap deflections of 0°, 20°, 30°, 35°, 40° and 60° were tested at various angles of attack from 0° to 37°. It is quite clear from these tests that, under certain conditions, extremely unstable hypersonic flow patterns are formed.

Prominent spectral energy peaks ranging between 1200 to 2200 Hz also were observed which could be correlated directly with large unsteady flow fields. The presence of unstable flow conditions was found to be strongly dependent on the presence of multiple shock interactions and their position relative to the location of the reattaching shear layer.

INTRODUCTION

The extension of the maneuvering capabilities of conventional aircraft to space shuttle vehicles probably will require the use of high cross-range lifting bodies equipped with heat-resistant control surfaces. It is particularly important that such vehicles and their deflected control surfaces be free of aerodynamic and aeroelastic instabilities through all speed ranges. Such instabilities are difficult to predict and are not the focus of the usual test program; hence, specific programs must be designed to meet this need.

A basic feature of the steady flow pattern about control surfaces at hypersonic speeds is the appearance of a separated pocket ahead of a deflected flap. The general character of this pattern is presented in figure 1. Behind the bow shock, the boundary layer thickness on the body surface increases until, at some point A in front of the flap, the boundary layer separates. A separated dead air pocket is formed as the boundary layer again reattaches at point B on the flap. Although the flow in the pocket often is

characterized as dead air, it may, in fact, be unsteady and, for certain configurations, contain considerable cross flow. The steady flow pattern falls into several categories, depending on whether the separated boundary layer is fully laminar, has transition occurring between the separation and reattachment lines, or is fully turbulent. For ideally two-dimensional cases with high flap deflections, the flow may attach at the trailing edge of the flap; but, in general, reattachment takes place ahead of the trailing edge.

In either supersonic or hypersonic flow, the separated boundary layer will turn through an oblique reattachment shock at point B, provided the flap angle is not too great. As the flap angle increases, point B moves toward the trailing edge until, at some angle, the shock can no longer remain attached, and the flow is forced to turn through a detached shock. For certain geometries the bow shock and detached flap shock will intersect in the vicinity of the flap. From this intersection a shock may then originate which will interact directly with the separated boundary layer on either the flap or the body surface. Such interactions can give rise to phenomena which transcend the problems of control surface oscillations and engage the much broader question of the stability of separated pockets perturbed by oscillating shocks.

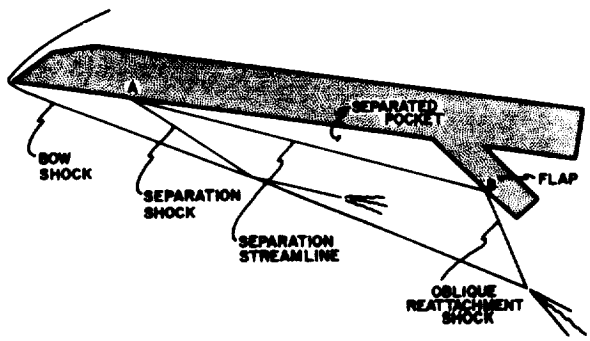

Figure 1. - Flow pattern at hypersonic speeds.

Although considerable theoretical and experimental work now exists concerning the steady flow aspects of hypersonic separated flows (e.g., Proceedings of the AGARD Conference on Separated Flows, reference 1), little information exists on the unsteady aerodynamics of configurations with regions of separated flow. The separated flow pocket is, in fact, often unstable and thus is a likely contributor to oscillatory control surface instabilities. It should be noted that separated flows, especially with a transitional or turbulent shear layer, generally are unsteady, even for "clean" configurations such as flow into a forward-facing step. References 2 and 3 state that the separated flow up a step is unsteady, but they do not give any quantitative data on this point. Reference 4 gives a wealth of data for Mach numbers 3 and 4.5, showing pressure fluctuations significantly larger than those produced for an attached boundary layer, and they offer persuasive arguments for the conclusion that the instantaneous location of the separation point moves about at a relatively low frequency. An excellent example of an instability occurring in the separated pocket of a spiked cone in high-speed flows is given in references 5 and 6.

The results of a number of early wind tunnel investigations (refs. 7 and 8) seemed to indicate that control surface instabilities of lifting body configurations could occur at hypersonic speeds. Since these results were subjectively inconclusive, an exploratory wind tunnel investigation was undertaken by Goldman (ref. 9) to obtain some insight into aeroelastic mechanisms that might lead to undesirable hypersonic control surface oscillations on typical lifting body re-entry configurations. As reported in reference 10, it was found that the oscillations that do occur involve a complex interaction between flow separation, free stream disturbances and vehicle geometry. Perhaps the most unusual aspect of the phenomenological observations made during these experiments was the occurrence of a large irregular buzz type excitation of the flow field when the bow shock on an M-1 type model interacted with the separation associated shocks on the flap. The excitation appeared to be a purely aerodynamic type of instability that did not depend on the flexibility or natural frequency of the flap. This somewhat spectacular hypersonic buzz instability was clearly related to an unsteady interaction between the bow shock and the separation/reattachment shocks.

These observations are similar to those noted in separate high Mach number experiments on the M-1 configuration by Holdaway, Polek and Kemp (references 11 and 12) and by Stern and Rowe (reference 13) during tests to determine the effect of gap size on pressures over a flap on a blunt delta wing in hypersonic flow.

Goetz, on the other hand, in an experimental investigation of control surface instabilities at a Mach number of 15.4 (ref. 14), discovered a destabilizing trend related solely to the loss of aerodynamic control surface damping for increasing flap angles. This observation would tend to indicate that flap motion plays a significant role in the aerodynamic feedback path. It also introduces the possibility of a number of additional phenomenological considerations involving aeroelastic instability mechanisms.

The phenomena observed to date are of sufficient magnitude to be important in the design of a re-entry vehicle. It is quite clear that shuttle vehicles must be free from the forces associated with strong unstable shock interactions and that these vehicles cannot risk being exposed to potentially dangerous flow instabilities. If a correct model for this instability can be obtained, the chances of designing to avoid it are enhanced. In this respect, the possibility of further clarification and classification of this mechanism suggested that additional experiments were warranted. Accordingly, the present experimental study was undertaken in order to obtain a better understanding of the unstable shock interaction phenomenon on a deflected control surface at hypersonic speeds. Its purpose was to explore experimentally the instability mechanism through a detailed evaluation of the aerodynamic nature of the phenomenon and its relationship to multiple shock interactions.

SYMBOLS

f	frequency, Hz
L	reference length, model length, 35.56 cm (14.00 in.)
M	Mach number
p	pressure, psi
$\bar{p}^2$	mean square value of fluctuating pressure, psi^2
q	dynamic pressure, newton/$meter^2$ (psi^2)
$\overline{S(f)}$	ensemble averaged power spectral density of pressure fluctuations, psi^2 per Hz
T	absolute temperature, °K
x	axial distance from model nose
y	lateral distance from model centerline
α	angle of attack, degrees, referenced from the horizontal (see figure 2)
β	flap deflection, degrees, referenced from the body (see figure 2)
ε	bow shock angle, degrees
ξ	x/L
η	y/L

Subscripts

ℓ	local conditions
T	total conditions
∞	free-stream conditions

APPARATUS AND PROCEDURES

Experimental Arrangement

The experiments were conducted in the Mach 20 leg of the Langley high Reynolds number helium tunnel. The facility, described in reference 15, operates by exhausting from a high pressure helium storage supply through an inlet nozzle, test section and diffuser into two large vacuum spheres. A typical run time, not including start-up and shutdown, is about 4 seconds. Although the tunnel's test section is 152.4 cm (60 in.) in diameter, the relatively thick hypersonic turbulent boundary layer that builds up on the test section's walls reduces the usable inviscid flow test region to a core size of about 51 cm (20 in.) in diameter.

The requirements for the use of this specific facility were dictated by Mach number, Reynolds number and stagnation temperature considerations as well as a compelling desire to establish flow conditions on the model that, based on past experience, would lead to or at least encourage strong shock interactions. In addition, the operating performance and specialized flow visualization capabilities of the tunnel met the basic needs of the test program's objectives. Most of the tests were conducted at a Mach number of about 17.5, a stagnation pressure around 550 N/cm^2 (800 psi) and a stagnation temperature close to 300°K (540°R). At these conditions, the speed of sound in helium is approximately 100m/sec (330 ft/sec). The resulting free stream Reynolds number of 15×10^6 per m (3.8×10^5 per in.) was sufficiently high that the transitional separation of the boundary layer flow on the model surface was anticipated.

Model and Test Conditions

The stainless steel model, shown in figure 2, has the general appearance of a high cross-range shuttle configuration accentuated to a great degree by a large flap on the lower surface. The overall model length of 35.56 cm (14.00 in.) and maximum width 27.94 cm (11.00 in.) represents approximately a 1:100 scale of a shuttle configuration and was selected on the basis of tunnel blockage considerations and the desirability of keeping the model well within the region of the tunnel's inviscid test core. The model design was roughly patterned after the configuration used by Stern and Rowe (ref. 13) in their tests to determine the effect of gap size on mean static pressures along the flap of a blunt delta wing in hypersonic flow. It was expected that the unanticipated observations made by Stern and Rowe of a large unsteady shock interaction phenomenon at Mach 10 in air could be duplicated effectively at Mach 17.5 in helium.

To keep the bow shock close to the forebody (i.e., to minimize the characteristic large bow shock standoff inherent in helium testing), the model bluntness was reduced by machining a 45° chamfer around the leading edge of the forebody. The flap was interconnected to the forebody through a stiff

angular fitting and was adjustable to flap angle settings of 0°, 20°, 30°, 35°, 40° and 60°. The angular fitting essentially provided a flap rotational stiffness of sufficient magnitude to yield flap resonances, summarized in Table I, that were all well above the design goal of 500 Hz. A nylon seal at the leading edge of the flap was included in the design in order to eliminate flow through the narrow gap between the flap leading edge and the forebody.

TABLE I. - FLAP RESONANT FREQUENCIES

β	Frequency
deg.	Hz
20	2050
30	1200
35	1250
40	1150
60	800

The model was located in the center of the tunnel's test core as shown in figure 3. A separate 45.72 cm (18.00 in.) angled sting adapter (angled at 20°) was fabricated to bridge the gap between the model and the long tapered sting attached to the tunnel's angle of attack quadrant. The angle of attack range of this quadrant was about +17° to -20°, with its center of rotation located on the model's sting adapter in the position shown in figure 2. Using the quadrant and the sting adapter, the model angle of attack could be varied anywhere from 0° to 37°.

The actual test conditions covered a full range of flap angles and angle of attack variations including a limited number of tests run at reduced stagnation pressures. Table II summarizes the tunnel flow parameters, flap angles and angle of attack settings for each of the test runs.

Instrumentation

Surface-pressure fluctuations. Perturbations in the surface pressures on the model forebody and flap were measured by a series of 22 miniature differential pressure transducers located in the positions indicated in figure 2. The transducers were similar to those used in the boundary layer pressure fluctuation studies of references 16 and 17. The sensors, which were 3.2 mm

in diameter, consisted of 2.2 mm circular diaphragms connected to fully active, four-arm semiconductor strain gage bridges. The development, use and limitations of these transducers is discussed in some detail in reference 18.

To obviate the undesirable consequences of a protruding transducer (see reference 17), the sensor diaphragms were purposely depressed .25 mm below the exposed surface through a 1.0 mm circular opening. The sensor bridges first were connected to individual direct current power supplies and amplifiers. The mean static pressure component of the signal was removed from the output by coupling the signal to a magnetic tape recorder through an alternating-current amplifier. Frequency-modulated recording at a center frequency of 108 KHz subsequently was carried out at a tape speed of 60 in/sec. The frequency response of the resulting overall system was essentially flat from 0.5 Hz to 200 KHz.

The reference tube on the back of each sensor was connected to a relatively large, internal manifold whose pressure could be externally adjusted and set. During a test run, the reference pressure could be fixed at a constant pressure or connected through a long tube to the tunnel's static pressure port.

Mean static pressures. Static pressures for the purpose of defining the pressure distributions ahead of the flap were taken at the 10 locations shown in figure 2. These static pressures were transmitted through 1.0 mm orifices in the forebody to tubing leading to slow-response differential pressure transducers located inside the model and the quadrant sting. Tubing runs were kept short (no longer than 90 cm) to allow for pressure stabilization within the available run time (ref. 19). Transducer reference pressures were maintained by manifolding in the manner previously described for the pressure fluctuation transducers. Time-averaged signals from these transducers were appropriately amplified, converted to static pressures and digitally recorded by the facility's computer system.

Flow Visualization

Schlieren photography. The pattern of unsteady shock interactions and their associated separated flow fields were monitored by two separate high-speed schlieren systems. The first system used a multiple still camera arrangement especially designed for examining fluctuating flows. Three sequential spark schlieren photographs were taken using illumination provided by three air gap sparks. Each spark light source was connected to a common triggering device that controlled the spark sequence through an adjustable delay network. The spark duration was less than 0.3 μsec. Auxiliary optics eliminated optical interference and minimized each camera's viewing position error to less than 0.1°. In all other aspects, the system was conventional, although special consideration had been given to the choice of mirrors and optics in order to provide optimization in both photographic sensitivity and resolution.

The second system involved the use of a high-speed 35-mm motion picture camera and a high-intensity xenon lamp continuous illumination source. The framing rate for these motion pictures was adjusted for a maximum speed of 6000 frames/sec. The framing camera's schlieren system used the same mirrors as the multiple spark system; however, a difference in offset position eliminated optical interference.

Oil flow tests. Flow separation and reattachment often can be observed best through the use of oil streak photography. Although it was not possible to conduct oil flow tests in the Langley Mach 20 high Reynolds number helium tunnel, equipment for such tests was available in the nearby Langley Mach 20 22-inch helium hypersonic blowdown tunnel. To take advantage of this flow visualization capability, a series of oil flow tests were conducted in the 22-inch tunnel using a scaled-down wooden model of the larger stainless steel configuration. The selected scale factor of 0.367 was based on the ratio of tunnel sizes. The oil flow model had a 40° flap deflection and was tested at angles of attack of 1°, 10°, 20°, 30° and 39°. Oil streak photographs were obtained for the area ahead of, around, and perpendicular to the deflected flap.

Data Reduction

Spectral Analysis. Power spectral densities of the surface pressure fluctuations were obtained by passing the tape recorded transducer signals through a high-speed digital processor. The processor used the digital Fourier transform techniques and sampling algorithms for analyzing random data described by Bendat and Piersol in reference 20.

In the present application, selected portions of the 60 in/sec frequency-modulated tape signals from the 22 pressure transducers first were demodulated and recorded on separate tape loops* at 15 in/sec. This speed reduction provided the frequency scaling needed to make the desired analysis range of 20 KHz compatible with the 5 KHz upper limit of the digital processor. The tape loop signals subsequently were cut off above 5 KHz (to eliminate foldover errors), sampled at 10,000 samples per second and analyzed in a time-series digital routine to produce ensemble-averaged power spectral densities of surface pressure fluctuations.

The effective bandwidth of the resulting digital output was 40 Hz and had a statistical reliability above 200 Hz of approximately 2 db 96% of the time. The resulting discrete digital power spectral density values were appropriately filtered, smoothed and reproduced on a logarithmic plotter in the form of $(psi)^2/Hz$ versus frequency in Hz.

Root mean squared pressures. The root mean squared values of the surface pressure fluctuations were obtained by passing the tape loop output signals through an acoustic sound pressure level meter. A high-pass 100 Hz filter was used in this sytem to eliminate low frequency noise and hum. Transducer gain settings in the tunnel originally were selected for a maximum anticipated signal sound pressure level of 180 db. Laboratory tests indicated that, at this setting, the total instrumentation noise level (including amplifiers, cables, recorders, etc.) was approximately 50 db down. In interpreting the data, sound pressure levels below 136 db were considered to be unacceptable and in most cases were discarded.

* The tape loop covered approximately 3 seconds of real time data.

RESULTS AND DISCUSSION

Experimental Overview

Before the quantitative results are presented and discussed in detail, it will be of value to give an overview of the flow field as obtained from the high-speed schlieren motion pictures, schlieren still photos and oil flow photographs. Although the motion pictures cannot be presented here, this medium proved to be one of the most valuable tools for providing a general perspective of the flow phenomena and the parametric boundaries within which large-scale oscillatory instabilities occurred. Tunnel starting requirements dictated that the model be raised to the test point shortly after flow initiation. Since this starting procedure was filmed, one can observe, for a fixed flap deflection, the flow development with increasing angle of attack. An impression of such development can be obtained for various flap deflections from the mosaic of schlierens shown in figure 4. Each of the test conditions studied is presented there.

Consider now the sequence of photographs in figures 5(a) through 5(g). The flap deflection angle, β, is fixed at 40°, while the angle of attack, α, varies from 0° to 37°. (The terminology which will be used in the later discussion is defined here in these first few photographs.)

At $\alpha = 0°$ (fig. 5(a)) the bow shock passes below the flap. A laminar boundary layer (L.B.L.) can be seen separating from the body very close to the nose at a slight angle to the body. The separating layer produces a series of compression waves which coalesce into a weak separation shock just inside the bow shock. Reflection of this weak shock from the bow shock occurs at S. The separated shear layer, which seems to maintain its laminar structure, reattaches through a shock close to the flap trailing edge.

At $\alpha = 10°$ (fig. 5(b)) the steeper density gradients accentuate the previously discussed features. In particular, the separated laminar shear layer now is clearly visible and undergoes transition about midway between separation and reattachment. The point of reflection, S, now occurs much closer to the nose, and the reflected shock can be seen intersecting the shear layer near the beginning of its transition. The reattaching shear layer turns through an oblique shock, moves along the flap for a short distance, and is further compressed by an impinging shock. This shock originates from the intersection, I, of the leading edge shock and the detached shock caused by the flap. The unintercepted portion of the impinging shock can be seen beyond the leeside of the flap. Even with this complexity, however, the oscillations of the shock structure were small.

For the flow condition at $\alpha = 20°$ (fig. 5(c)) the increasing angle of attack causes the separated shear layer to lie much closer to the body, and the reflection point S has moved back along the bow shock. The shock emanating from point I now impinges the flap in the immediate vicinity of the reattachment point. At the lower angles of attack, the reattaching layer and the impinging shock were slightly unsteady and exhibited small excursions

about a mean position. With increasing angle of attack, these small excursions overlap, and the oscillations become very large.

With further increase in angle of attack, $\alpha = 25°$, $30°$ and $33°$ (figs. 5(d), 5(e) and 5(f), the impinging shock moves upstream of the reattachment point on the flap and intersects the shear layer prior to reattachment. In this range of angles of attack, the impinging shock exhibited excursions up to 25% of the flap chord. Finally, at $\alpha = 37°$ (fig. 5(g)), the impinging shock has moved onto the forebody, and the high-speed motion pictures show that the oscillation amplitudes have actually decreased.

The schlieren and high-speed motion pictures lead to a two-dimensional conceptualization of the flow. But, a more realistic viewpoint is provided by the set of oil flow photographs, shown in figure 6, which provide a reminder of the richness of the three-dimensional flow phenomena under consideration. The flap deflection in this sequence was fixed at $\beta = 40°$, while the angles of attack are 1°, 20°, 30° and 39°.

In figures 6(a) and 6(b), it can be seen that the separation line moves closer to the nose with increasing angle of attack (although not shown here, the separation line for $\alpha = 10°$ was intermediate between these two positions). Further increase in angle of attack results in the rearward movement of the separation line shown in figures 6(b) and 6(d).

The forward and rearward movement of the separation line is the result of two opposing mechanisms, one of which ultimately overcomes the other. Initially, as α increases, the first mechanism dominates and the separation line moves forward. Beyond $\alpha = 20°$, the second mechanism dominates and the separation line moves rearward. Forward movement of the separation arises from the flap intercepting an increasing portion of the separated shear layer as the model moved away from the 0° angle-of-attack position; this can be seen in figures 5(a), 5(b) and 5(c). Rearward movement of the separation line is encouraged by cross flows, which increase with angle of attack (as indicated in the oil flow photographs) and decrease the size of the separated pocket.

Reattachment occurs initially, close to the flap trailing edge and, with increasing α, moves steadily toward the hinge line. Near the flap tips, a swirling pattern appears for all angles of attack as the flow sweeps off the flap tips in two trailing vortices.

To summarize: with $\beta = 40°$ and $\alpha = 0°$, the high-speed motion pictures indicate that the shock wave and flow field surrounding the body are generally steady, although tunnel flow fluctuations cause an occasional tremor. As the angle of attack increases, some unsteadiness occurs, but the level remains low. As α passes through 20° and beyond, the entire scale of oscillation changes. The impinging shock, appearing as a white line in the films, resembles an electric discharge arc dancing back and forth along the flap, and the entire flow structure oscillates wildly. At the maximum angle of attack, the impinging shock has progressed to the forebody and now, although the oscillation still is severe, it has decreased from its maximum.

At low angles of attack (i.e., $\alpha = 1°$), the separated pocket appears

quiescent, and a substantial surface region appears to have been subjected to almost no shear. With increasing angle of attack (i.e., $\alpha > 20°$), the shear increases, and considerable cross-flow develops.

Tests were also undertaken at reduced stagnation pressures (p_t = 260 N/cm^2) for $\beta = 40°$ in the anticipation of finding some effect on the flow field due to a change in Reynolds number. No significant change in the instability pattern was, however, observed and the results were more or less repetitious of the tests conducted at the higher stagnation pressures. As indicated in the section on Instrumentation, measurements were also made of the static pressures on the model forebody in the off centerline positions shown in figure 2. It had been hoped that these measurements would be useful in locating the extremities of the separated pocket and in eventually defining the pocket size. As was later discovered the three-dimensional effects, especially the large cross flows, were quite strong and the resulting static pressure measurements provided little assistance in understanding the flow phenomena. Since neither the reduced stagnation pressure tests nor the static pressure data appeared to provide any significant insight into the problem under consideration, they have not been included in the discussion.

Effect of Flap Deflection, $\beta = 40°$

The sequence of curves in figures 7 through 11 are the test values of power spectral densities obtained from the centerline pressure transducers for $\beta = 40°$. In each figure, the ordinate has been nondimensionalized by the square of the local dynamic pressure, q_ℓ^2. The ordinate scale is uniform for all figures so that a visual impression of the unsteady pressure variations along the centerline may be obtained. Similarly, the root mean square (rms) pressure distributions along the centerline of the forebody and flap referenced to the local dynamic pressure, q_ℓ, are presented in figure 12. Values of q_ℓ were based on measurements of the bow shock angle, ϵ, at each angle of attack and the corresponding analysis provided by the helium flow tables of reference 21. ϵ was determined directly from the still camera schlieren photographs. A summary of results of these calculations is provided in Table III. Location of the separation point and reattachment point estimated from the oil flow photographs are listed in Table IV and indicated on figure 12. The rms levels for each transducer are also listed in Table V.

In what follows, particular attention will be paid to the occurrence of energy spikes and the general spectral shape of figures 7 through 11. These will be discussed in conjunction with the schlieren photographs, figures 5(a) to 5(g), and the oil flow photographs, figures 6(a) to 6(d), as well as the rms pressure distributions in figure 12. In this way, phenomena may be correlated among the different information modes, and a more complete description obtained.

The data for the $\beta = 40°$ configuration generally are representative of the growth of the large amplitude oscillations previously described. The flow field behavior about flaps that were deflected 30° and 35° differed only quantitatively and will not be discussed here. Extraordinary results and other salient points, however, will be discussed separately.

$\underline{\alpha = 0°}$. The power spectral densities for this condition are shown in figure 7. Each transducer spectrum contains a spike at approximately 1250 Hz. These spikes are particularly prominent for the leading forebody transducers and the last two transducers (located within the reattachment region). The transducer locations and designations are shown in figure 2. The rms values for this run (see fig. 12) are relatively low and, as mentioned previously, are contaminated by system and amplifier noise. The low rms levels and the lack of energy in the spectrum above 1250 Hz suggest that the separated shear layer retains its laminar condition until near reattachment. The relatively featureless density gradient topography are shown in the schlieren photograph, figure 5(a), tends to support the view.

The laminar boundary layer separation, barely perceptible in figure 5(a), is located close to the nose. In the oil flow photograph, figure 6(a), this separation is at $\xi = 0.26$. The difference in location probably is due to the slight difference in the model's angle of attack, tunnel operating conditions, and the sensitivity of this phenomenon at $\alpha = 0°$. The relatively undisturbed oil dots indicate an extensive quiescent pocket. Reattachment occurs on the flap at $\xi = 0.96$ (approximately 83% of the flap chord).

$\underline{\alpha = 10°}$. The spectral characteristics for this test condition are presented in figure 8. Certain prominent features in the spectral densities are apparent; they include:

(1) An energy peak at about 2100 Hz appearing on the leading forebody spectra.

(2) The spectra upstream of the flap have considerably more energy in the frequency range between 1.5 to 20 KHz than they did for the $\alpha = 0°$ case.

(3) A large increase in the energy level at the last two transducers on the flap from the relatively low constant levels on the upstream transducers.

A careful comparison of the schlieren for this case (fig. 5(b)) with that of the previous $\alpha = 0°$ case (fig. 5(a)) indicates an earlier separation. The oil flow photograph shows that separation occurs at $\xi = 0.09$, and reattachment on the flap occurs at $\xi = 0.96$. After separation, the laminar shear layer undergoes transition in the vicinity of $\xi = 0.55$, which accounts for the enhanced energy content at higher frequencies relative to the $\alpha = 0°$ condition. The higher angle of attack gives rise to a detached normal shock (in front of the flap) that intersects the bow shock. From this intersection, an impinging shock is initiated toward the flap and is responsible for the very high 170-db sound pressure levels experienced at the last pressure taps (24 and 25). The intersection of these two shock surfaces envelops the flap and appears in the schlieren as a shock emanating from the leeside.

$\underline{\alpha = 20°}$. The salient features from the sequence of spectra presented in figure 9:

(1) An energy peak at 1250 Hz appears on the front five pressure taps.

(2) A leveling off of frequency distribution on pressure taps 6 and 9 due to an increase in high frequency content.

(3) An order of magnitude increase in energy levels between pressure taps 19 and 21.

(4) A peak value in rms levels at pressure tap 23 and then a decrease in rms levels toward the end of the flap.

Separation of the laminar boundary layer is estimated from the schlieren of figure 5(c) to occur at $\xi = 0.17$; but, from the oil flow photograph (figure 6(b)), it appears at $\xi = 0.12$. A weak shock orginates from the onset of the separation, reflects from the bow wave, and is observed to border the shear layer along the transition region. After the laminar shear layer separates, it undergoes transition in the vicinity of pressure taps 6 and 9 and is turbulent when reattachment occurs at $\xi = 0.90$. The impinging shock that emerges from the intersection of the detached flap shock and the leading edge shock encloses the flap and intersects it in the vicinity of tap 23 ($\xi = 0.80$) upstream of the reattachment point.

In the oil flow photograph (figure 6(b)) a well-defined separation line is evident near the nose. Along the center of the forebody, the flow is actually forward, with considerable cross-flow roughly normal to the swept leading edges. Reattachment occurs on the flap at the 61% chord point ($\xi = 0.90$), and the herringbone pattern suggests that two vortices are being shed from the tips of the flap.

$\underline{\alpha = 30°}$. This sequence of power spectral densities is shown in figure 10. A prominent spike does not appear on the spectra for the first two pressure taps, but it does occur on the third tap at a frequency of about 1400 Hz. The spike appears with varying prominence on all subsequent spectral signatures and occurs at a relatively low level at tap 23, which lies downstream of the reattachment point on the flap. The schlieren photograph (fig. 5(e)) indicates separation occurs between taps 2 and 3 at approximately $\xi = 0.31$. The appearance now of an initial peak on tap 3--not observed on taps 1 and 2--suggests that the appearance of a peak on a forward transducer may be an indication that the flow separated upstream of the pressure tap. Measurements from the oil flow photograph (fig. 6(c)), however, fix the separation on that model at $\xi = 0.35$, which would be slightly downstream of tap 3 ($\xi = 0.34$). This difference is quite small, considering the difference between the testing facilities. Nevertheless, although the existence of a spike seems to be associated with a separation, it is not clear whether a transducer slightly upstream of separation might not also register such a peak.

The spike also is present on the spectra from taps 25 and 26 downstream of reattachment, which, measured from the oil flow photographs, occurs at $\xi = 0.86$ or about 44% of the flap chord.

$\underline{\alpha = 37°}$. A rather broad energy peak now appears on the fourth tap at $\xi = 0.40$, while subsequent spectral signatures do not display the spikes of previous runs. Schlieren photographs (fig. 5(g)) indicate a rapid thickening of the boundary layer in the vicinity of $\xi = 0.46$ and transition immediately thereafter. The separated region is smaller, and the intersection of the bow

and detached flap shock has moved forward of the hinge. Oil flow (fig. 6(d)) indicates a reattachment at $\xi = 0.81$ and the turning shear layer appears to undergo a series of oblique shocks. Since the detached flap shock is near normal, a large subsonic flow field exists outside the turning supersonic shear layer.

Root mean square pressure distributions. The rms pressure distributions along the centerline of the forebody and flap are shown in figure 12(a) for the angles of attack discussed above. The pressure has been nondimensionalized by the local dynamic pressure, q_ℓ. Similar plots were made using the calculated local static pressure as a reference, but little difference in trend development was observed despite the different functional dependence of these two quantities on angle of attack.

As α increases from 0° to 20°, the maximum rms pressure increases and moves forward on the flap from its initial location at the trailing edge to almost mid-chord. The increase in maximum rms pressure is largest initially as the flap moves into the proximity of the bow shock. For $\alpha = 20°$, the maximum value of the non-dimensional rms pressure is equal to 0.27, while the ratio of q_ℓ to q_∞ is approximately 3.0. Hence, at reattachment, the rms pressure fluctuation can be as high as 0.8 q_∞. Such levels are beyond those observed by Holden (ref. 22) and are due at least in part to shock impingement phenomena of the type described by Edney in reference 23. Beyond $\alpha = 20°$, the peak continues to move forward on the flap and decreases in magnitude. The reattachment locations shown on the figure 12(a) are well correlated with the movement of the pressure peak.

At angles of attack, $\alpha = 30°$ and 37°, a rapid increase of pressure is followed by a plateau in the interval $0.4 \leq \xi \leq 0.65$. For these two runs, separation occurs in the vicinity of $\xi = 0.4$, and the transitional shear layer lies close to the body. This transitional shear layer probably is the cause of the high energy levels. For the lower angles of attack, separation occurs upstream of the first transducer (upstream of the second for $\alpha = 1°$). The shear layer now is located further away from the body and, as mentioned above, it appears laminar for the $\alpha = 0°$. Under these conditions, lower surface pressure fluctuations occur.

Effect of Flap Deflection, $\beta = 20°$

For this configuration, only the $\alpha = 20°$ condition will be discussed, because the phenomena encountered are representative of the other angles of attack. The high-speed motion pictures of these runs revealed no significant unsteadiness of the shock configuration. The schlieren photograph in the mosaic of figure 4 indicates a thickening boundary layer in the vicinity of tap 11 ($\xi = 0.62$). It is difficult to determine whether the thickening is an indication of the transition or incipient separation. The flow definitely is turbulent near the hinge, and it turns through an oblique shock on the flap. Existence of a turning shock close to the hinge line suggests that the separation region, if one exists, probably is quite small. As the flow proceeds

along the flap, it passes through the shock originating from the intersection of the flap and bow shocks.

The sequence of power spectral densities for this run, shown in figure 13, lack the narrow band energy peak that appeared to be associated with the separation of the laminar boundary layer for the $\beta = 40°$ configuration. Although broad maximums occur on the signatures of taps 9 through 13, there is no peaking on the flap, and the signatures appear to be similar to those of an attached turbulent boundary layer.

Effect of Flap Deflection, $\beta = 60°$

$\alpha = 0°$. The sequence of power spectral densities for the 60° flap configuration is shown in figure 14. The results differ considerably from those obtained for lower flap deflections. At lower flap deflections, the energy was distributed continuously over the spectrum and had occasional spikes at specific frequencies. Here, the energy is essentially periodic, partitioned by the digital processor into narrow spikes (the fundamental spike occurring at 1400 Hz, with higher harmonics at 2800, 4200 and 5600 Hz). The signal periodicity implied by the spectra is further demonstrated by the scope traces shown in figure 15.

The four schlieren photographs shown in figure 16 provide a visual impression of the unsteady motion of the bow shock accompanying the remarkable pressure spectra of figure 14. The photographs were selected from two runs with the same test conditions to provide an indication of the extent of the bow shock wave excursions. The high-speed motion pictures indicate that the bow shock position in the vicinity of the flap varied from the trailing edge, figure 16(a), to a distance away from the flap of about 2/3 the flap chord, figure 16(c). When the bow shock is close to the trailing edge, a normal shock forms, and the reattaching flow turns sharply, resulting in a high-pressure region at the trailing edge. When the bow shock is far from the trailing edge, the pressure in the shock layer is determined mainly by the oblique shock, and the pressure in this region is considerably less. As the pressure varies at reattachment, the amount of shear layer flow turned back to the pocket changes accordingly, and this changing flow, in turn, affects the location of the separation point. The effect near the nose of the model is considerable, as indicated by the large bow shock angular variations from figures 16(b) and 16(d).

A visual impression of the flow field at $\alpha = 10°$ and $\alpha = 20°$ can be obtained from the mosaic of schlierens of figure 4. The flow at these angles of attack also was extremely unsteady, as may be inferred from the unusual shape of the lower bow shock. Unsteadiness of the upper bow shock was also evident, but due presumably to the pocket pulsations transmitted to the vortices shed from the leading edges of such a delta wing configuration.

Root mean square pressure distributions. The rms pressure distributions for $\alpha = 0°$, 10° and 20° are shown in figure 12(b). The $\beta = 60°$ distribution differs from those discussed above in that sharply defined maxima appear at:

(1) $\xi = 0.21$, the first transducer

(2) $\xi = 0.70$, just forward of the hinge line

(3) $\xi = 1.00$, the trailing edge.

Between these maxima, relatively low rms values occur. As the angle of attack increases, the minimum rms values increase, and the distribution tends toward the shape characteristic of the lower flap angles (e.g., see figure 12(a) where $\beta = 40°$).

Boundaries of Large Oscillations

The data indicate that, while nearly all configurations exhibit some flow field unsteadiness, certain combinations of flap deflection and attack angle exhibit very large oscillations of the shock patterns and the flow field. These large amplitude oscillation conditions are indicated on the schlieren mosaic of figure 4 by the letter B. The categorization of the oscillations into this coded B grouping was heavily influenced by viewing the high-speed motion pictures and consequently is a matter of some judgment, especially for conditions near the boundary. Using the high-speed films as a guide, an attempt was made to find a less subjective means for obtaining evidence of large-scale oscillations. Necessary conditions for the presence of large oscillations were found to be:

(1) A separation pocket, which in most instances was associated with spikes in pressure power spectral densities.

(2) A shock wave emanating from the intersection of the bow shock and the detached flap shock that impinges on the flap.

But, these two conditions--alone or together--were not sufficient to cause large amplitude shock oscillations. Some examples for which the flow is separated without the presence of large oscillations are: $(\alpha,\beta) = (0°, 40°)$, $(0°, 35°)$, $(0°, 30°)$, etc. Similarly, the presence of an impinging shock or an impinging shock and a separation pocket were not sufficient for the cases where $(\alpha,\beta) = (20°, 20°)$, $(37°, 20°)$, $(10°, 40°)$, $(10°, 35°)$, etc. The condition of the separated shear in these examples could not be correlated with the presence of large oscillations (transition occurred for flows with both large and small oscillations). No correlation of the locus of the separation shock and its interaction with the shock system could be found to account for the oscillations.

In the mosaic of figure 4, it can be seen that under conditions of large oscillations, the shock originating at the intersection of the bow and flap shocks strikes the flap either upstream of, or in very close proximity to, the estimated reattachment of the separated shear layer. Conversely, when large oscillations were absent, there was much less intimacy between this impinging shock and the estimated shear layer reattachment region. In general, a small amount of unsteadiness of both the reattaching shear layer and the impinging shock always seemed to be present (the still schlieren photographs,

however, were not conclusive on this point).

To check this suspicion, the high-speed films for flap deflections, $\beta = 30°$, $35°$, and $40°$, and angle of attack, $\alpha = 37°$ were carefully scrutinized. For this angle of attack, tunnel flow was initiated with the model at 10°, and the onset of the large scale oscillations could be observed as the angle of attack increased. In each case, some unsteadiness of the impinging shock and the reattaching shear layer was seen when α was less than 15°. As α increased from 15° to 20°, the small unsteady excursions of the impinging shock (which moves up the flap) and the reattaching shear layer began to overlap, and the oscillations of the flow field increased significantly. As stated previously, these oscillations seemed to reach a maximum in the neighborhood of $\alpha = 30°$.

Estimates of the attack angle at which the oscillations began to grow are: $(\alpha,\beta) = (18°, 30°)$, $(16°, 35°)$, and $(15°, 40°)$. The conditions at which large oscillations occurred are indicated by the letter B in figure 4. No shock oscillations occurred for $\beta < 20°$, and, with the exception of $\beta = 60°$, oscillations did not occur for $\alpha < 10°$.

Relationship to Flap Frequencies

The previous discussion presented an argument to relate the observations of large unstable shock interactions to a purely aerodynamic feedback mechanism that is conceivably independent of the effects of flap motion. This argument is somewhat mitigated by the facts as shown in Table VI, that, except for the case of $\beta = 60°$, the prominent peaks in the pressure power spectral densities were not too far away from the measured flap resonant frequencies.

For the unstable angle of attack cases in which $\beta = 40°$, 35° and 30°, this frequency proximity could, of course, have been coincidental. The experimental results, however, do not permit such a conclusion. It is possible that the flap frequency acted in an incipient role by selecting the frequency at which the aerodynamic mechanism becomes unstable. Under this premise, one might assume that the unstable shock interactions have several characteristic frequencies that are dependent upon the separated flow pattern. The characteristic frequency that predominates may be the one triggered by--or closest to--the flap frequency.

If one of the characteristic aerodynamic frequencies is easily energized, the flap frequency might not play a significant role. In fact, this is what may have happened for the case in which $\beta = 60°$. For example, although the flap natural frequency was only 800 Hz, the strong instability at $\alpha = 20°$ had a very large peak in the pressure power spectral density at 2100 Hz.

The present results do not rule out a relationship between flap motion and an instability (nor do they suggest it). Since no attempt was made to measure flap frequency and damping during actual hypersonic flow conditions, comparisons cannot be made to verify the destabilizing trends in flap damping noted in reference 12. It is safe to surmise, however, that if the flap frequency were close to--or exactly coincided with--the unstable shock oscillation

frequency, one would expect a closely coupled highly unstable aeroelastic phenomenon.

CONCLUSIONS

Measurements of surface pressure fluctuations as well as flow visualization observations have been made in helium flow at a Mach number of 17.5 on the forebody and flap of a model representative of a high cross-range shuttle configuration. Within the confines of a selected range of aerodynamic and geometric parameters,it has been observed that the flow underlying the region of a deflected flap can be very unstable.

An experimental criteria for the existence of large scale unsteady oscillations was found to be related to the separation pocket bounded by its reattaching shear layer and a multiple shock interaction occurring near reattachment.

Three necessary conditions were found for the existence of these large scale oscillations.

(1) A sizeable separation region.

(2) The shock resulting from the intersection of the bow and flap shocks must impinge on either the body or the flap surface. Oscillation of the shock pattern, however, is greatest when impingement occurs on the flap.

(3) This shock must impinge in close proximity to, or upstream of, the shear layer reattachment. Within the flow and geometry conditions tested this last condition was also found sufficient.

Apparently, in this way, pressure fluctuations that accompany slight unsteady movements of the impinging shock can be fed back through the separated pocket, affect conditions at the separation point, and, therefore, modify the reattachment position of the separated shear layer. The details of this feedback mechanism are far from understood, and the present results do not rule out a role for flap motion in the mechanism. Nevertheless, the experience from the present study promises prospects for establishing general stability criteria for control surfaces.

No qualitative differences in these results were observed when the dynamic pressure was reduced 50%.

Although the angle of attack and flap deflection angles at which hypersonic buzz occurred exceed those anticipated for the shuttle ($\alpha = 35°$ and $\beta = 10°$), buzz is not expected to be limited solely to deflected control surfaces. The possibility for large scale oscillations should be examined whenever the interaction of an impinging shock and a reattaching shear layer seems likely. Given the complexity of the flow field about a shuttle configuration, such an interaction is probable.

REFERENCES

1. AGARD Conference Proceedings No. 4 - Separated Flows, AGARD Specialists' Meeting, Rhode-Saint-Genese, Belgium, May 1966.

2. Chapman, D.R.; Kuehn, D.M.; and Larson, H.K.: Investigation of Separated Flows in Supersonic and Subsonic Streams with Emphasis on the Effect of Transition. NACA TN 3869, 1957.

3. Bogdonoff, S.M.: Some Experimental Studies of the Separation of Supersonic Turbulent Boundary Layers. Papers presented at the Heat Transfer and Fluid Mechanics Institute. UCLA, sec. V, June 1955, pp. 1-23.

4. Kistler, A.L.: Fluctuating Wall Pressure under a Separated Supersonic Flow. J. Acoust. Soc. Am., vol. 36, no. 3, Mar. 1964, pp. 543-550.

5. Maull, D.J.: Hypersonic Flow over Axially Symmetric Spiked Bodies. J. Fluid Mech., vol. 8, 1960, pp. 584-592.

6. Wood, C.J.: Hypersonic Flow over Spiked Cones. J. Fluid Mech., vol. 12, 1962, pp. 614-624.

7. Widmayer, E., Jr.: Aerodynamic Excitations of Flaps at M=16. Rep. No. 2025-38, Martin Co., Sept. 1961.

8. Widmayer, E., Jr.: Preliminary Investigations of the Aerodynamic Excitation of Flaps at Hypersonic Speeds. RM-159, Martin Marietta Corp., Aug. 1963.

9. Goldman, R.L.: Investigation of Control Surface Instabilities of Lifting Body Configurations. AFFDL-TR-65-106 (CONFIDENTIAL), Nov. 1965.

10. Goldman, R.L.; Morkovin, M.V.; and Schumacher, R.N.: Unsteady Control Surface Loads of Lifting Re-Entry Vehicles at Very High Speeds. AIAA, vol. 6, no. 1, 1968, pp. 44-50.

11. Holdaway, G.H.; Polek, T.E.; and Kemp, J.H., Jr.: Aerodynamic Characteristics of a Blunt Half-Cone Entry Configuration at Mach Numbers of 5.2, 7.4 and 10.4. NASA TMX-782 (CONFIDENTIAL), 1963.

12. Kemp, J.H., Jr.; Holdaway, G.H.; and Polek, T.E.: Characteristics of an Aerodynamic Control System for Use with Blunt Entry Configurations at Mach Numbers of 10.7 and 21.2 in Helium. NASA TM X-1153 (CONFIDENTIAL), 1965.

13. Stern, I.; and Rowe, W.H., Jr.: The Effect of Gap Size on Pressure over the Flap of a Blunt Delta Wing in Hypersonic Flow. Reprint No. 66-408, AIAA Fourth Aerospace Sciences Meeting, Jan. 1966.

14. Goetz, R.C.; and Gibson, F.W.: Investigation of Control-Surface Instabilities on Lifting-Body Re-Entry Vehicles at a Mach Number of 15.4. NASA TN D-6301, 1971.

15. Watson, R.D.; and Bushnell, D.M.: Calibration of the Langley Mach 20 High Reynolds Number Helium Tunnel Including Diffuser Measurements. NASA TM X-2353, 1971.

16. Chyu, W.J.; and Hanly, R.D.: Power- and Cross-Spectra and Space-Time Correlations of Surface Fluctuating Pressures at Mach Numbers between 1.6 and 2.5. NASA TN D-5440, 1969.

17. Coe, C.F.: Surface-Pressure Fluctuations Associated with Aerodynamic Noise. Basic Aerodynamic Noise Research, NASA SP-207, 1969, pp.409-424.

18. Kicks, J.C.: Development and Application of Ultra-Miniature Pressure Transducers for Use in Wind Tunnel Models Section Two. Paper presented at the 15th International ISA Aerospace Instrumentation Symposium (Las Vegas, Nev.) May 1969.

19. Volluz, R.J.: Handbook of Supersonic Aerodynamics. Sec. 20. Wind Tunnel Instrumentation and Operation. NAVORD Report 1488, vol. 6, Jan. 1961.

20. Bendat, J.S.; and Peirsol, A.G.: Random Data: Analysis and Measurement Procedures. John Wiley and Sons, Inc., 1971.

21. Mueller, J.N.: Equations, Tables, and Figures for Use in the Analysis of Helium Flow at Supersonic and Hypersonic Speeds. NACA TN 4063, 1957.

22. Holden, M.S.: Shock Wave-Turbulent Boundary Layer Interaction in Hypersonic Flow. Reprint No. 72-74, AIAA 10th Aerospace Sciences Meeting, Jan. 1972.

23. Edney, B.E.: Effects of Shock Impingement on the Heat Transfer around Blunt Bodies. AIAA, vol. 6, no. 1, Jan. 1968, pp. 15-21.

TABLE II

SUMMARY OF TEST CONDITIONS

Run	α	β	p_T	T_T	M_∞
	Deg.	deg.	N/cm^2	°K	
1-20	0	0	539	308	17.43
1-21	20	0	552	307	17.44
1-23	30	0	550	306	17.84
1-24	37	0	547	303	17.87
1-26	0	20	536	301	17.44
1-27	20	20	536	302	17.44
1-28	30	20	546	301	17.44
1-29	37	20	534	299	17.45
1-30	0	40	545	301	17.44
1-31	20	40	546	298	17.47
1-32	30	40	545	296	17.45
1-33	37	40	545	295	17.43
1-34	0	40	267	298	16.58
1-35	20	40	264	298	16.57
1-36	30	40	265	296	16.57
1-37	37	40	266	295	16.58
2-1	0	20	559	290	17.53
2-2	10	20	557	288	17.50
2-3	20	20	557	288	17.50
2-4	30	20	557	287	17.52
2-5	37	20	556	289	17.53
2-6	10	40	550	298	17.43
2-7	20	40	552	292	17.45

Run	α	β	p_T	T_T	M_∞
	deg.	deg.	N/cm^2	°K	
2-8	25	40	552	290	17.41
2-9	30	40	553	290	17.43
2-10	10	40	553	286	17.43
2-11	33	40	553	289	17.41
2-12	37	40	552	288	17.41
2-13	0	30	555	301	17.43
2-14	25	30	554	296	17.41
2-15	30	30	554	296	17.41
2-16	33	30	554	296	17.41
2-17	37	30	554	293	17.41
2-18	20	30	553	290	17.39
2-19	0	35	551	292	17.53
2-20	10	35	553	292	17.52
2-21	25	35	552	292	17.52
2-22	30	35	552	291	17.49
2-23	33	35	552	289	17.52
2-24	37	35	552	288	17.48
2-25	20	35	551	285	17.49
2-26	0	60	550	295	17.53
2-27	10	60	553	295	17.55
2-28	20	60	553	292	17.48
2-29	0	60	554	290	17.53

TABLE III

LOCAL FLOW CONDITIONS

α	ϵ	M_ℓ	p_ℓ	q_ℓ
deg.	deg.		N/cm^2	N/cm^2
0	7.2	11.3	.030	3.25
10	13.1	7.11	.109	4.24
20	24.9	3.80	.349	4.21
25	29.6	3.14	.484	3.91
30	35.0	2.55	.657	3.56
33	38.8	2.25	.780	3.28
37	44.0	1.89	.952	2.89

TABLE IV

SEPARATION AND REATTACHMENT LOCATIONS

FOR $\beta = 40°$

α	Separation	Reattachment	
deg.	ξ	ξ	% Flap Chord
1	0.260	0.958	83.2
10	0.092	0.958	83.2
20	0.115	0.902	60.8
30	0.354	0.860	44.0
39	0.434	0.807	22.8

TABLE V

ROOT MEAN SQUARED PRESSURES, ($\bar{p}^2/q_\ell$) x 10^2

FLAP	β = 0°				β = 20°					β = 40°							ξ
RUN	1-20	1-21	1-23	1-24	1-26	2-2	1-27	1-28	1-29	1-30	2-6	1-31	2-8	1-32	2-11	1-33	
Tap \ α	0°	20°	30°	37°	0°	10°	20°	30°	37°	0°	10°	20°	25°	30°	33°	37°	
1	0.19	0.34	0.71	1.16	0.19	0.25	0.34	0.75	1.16	.26	.47	.95	.65	.75	1.10	1.16	.210
2	0.25	0.36	0.75	1.16	0.19	-	0.36	0.75	1.23	.29	-	.90	-	.75	-	1.23	.274
3	0.19	0.36	0.75	1.23	0.21	0.22	0.34	0.75	1.30	.21	.47	.90	1.62	1.19	1.45	1.38	.337
4	0.19	0.36	0.75	1.30	0.19	0.24	0.36	0.75	1.30	.23	.47	1.01	1.62	1.99	2.18	2.19	.401
5	0.22	0.38	0.79	1.38	0.26	-	0.36	0.79	1.38	.29	-	1.20	-	2.24	-	2.76	.465
6	0.19	0.34	0.75	1.30	0.21	0.25	0.45	0.75	1.55	.25	.78	1.42	3.05	4.46	5.79	5.82	.528
9	0.31	0.40	0.79	1.46	0.29	0.25	0.64	1.12	2.19	.35	.66	1.90	3.23	4.21	5.46	5.50	.582
11	0.19	0.36	0.75	1.46	0.19	-	0.64	1.33	2.32	.33	-	2.13	-	4.21	-	5.50	.617
13	0.19	0.40	0.84	1.55	0.19	0.22	0.71	1.58	2.76	.31	.50	2.53	3.84	5.01	5.79	6.53	.653
15	-	-	-	-	-	0.15	-	-	-	-	.30	-	3.23	-	5.16	-	.689
16	-	-	-	-	-	0.25	-	-	-	-	.83	-	5.75	-	7.72	-	.759
18	-	-	-	-	-	0.33	-	-	-	-	.66	-	8.12	-	13.0	-	.795
19	0.21	0.36	0.84	1.46	0.25	-	4.01	4.21	7.33	.29	-	9.50	-	14.12	-	15.49	.812
20	0.31	-	-	-	-	0.21	-	-	-	-	.53	-	10.83	-	17.3	-	.831
21	0.25	0.40	0.89	1.46	0.28	-	2.68	4.46	6.92	.35	-	14.22	-	25.10	-	17.39	.848
22	-	-	-	-	-	0.37	-	-	-	-	1.40	-	21.61	-	17.3	-	.866
23	0.29	0.38	0.84	1.46	0.35	-	2.13	5.62	4.90	.39	-	26.78	-	21.12	-	9.23	.884
24	-	-	-	-	-	2.49	-	-	-	-	9.92	-	20.40	-	14.5	-	.902
25	0.31	0.45	0.94	1.46	0.39	3.73	2.68	3.16	3.89	.82	15.72	11.29	15.3	13.33	9.72	4.90	.939
26	0.44	0.42	0.89	1.38	0.41	-	5.34	1.41	2.19	1.23	-	6.73	-	6.68	-	3.27	.976
27	-	-	-	-	-	-	-	-	-	-	-	-		-	-	-	
28	0.26	0.42	0.89	1.46	0.39	-	2.68	5.62	5.50	.62	-	20.08		25.10	-	11.62	

TABLE V - Continued

ROOT MEAN SQUARED PRESSURES, ($\bar{p}^2/q_\ell$) x 10^2

FLAP	β = 30°						β = 35°							β = 60°			
RUN	2-13	2-18	2-14	2-15	2-16	2-17	2-19	2-20	2-25	2-21	2-22	2-23	2-24	2-26	2-27	2-28	ξ
Tap \ α	0°	20°	25°	30°	33°	37°	0°	10°	20°	25°	30°	33°	37°	0°	10°	20°	
1	0.39	0.47	0.65	0.89	1.09	1.38	0.28	0.35	0.50	0.61	0.84	1.03	1.30	2.31	1.18	1.76	.210
2	-	-	-	-	-	-	-	-	-	-	-	-	-	-	-	-	.274
3	0.19	0.67	0.54	0.84	1.03	1.38	0.26	0.33	0.90	1.02	1.06	1.15	1.38	1.55	1.11	2.53	.337
4	0.26	0.85	0.91	1.00	1.22	1.38	0.22	0.31	0.90	1.44	1.78	1.94	1.95	1.23	1.11	3.00	.401
5	-	-	-	-	-	-	-	-	-	-	-	-	-	-	-	-	.465
6	0.25	1.01	1.53	2.11	2.44	2.76	0.26	0.37	1.13	1.82	2.66	3.25	3.89	1.03	1.48	3.57	.528
9	0.22	1.01	1.72	2.66	3.65	4.73	0.26	0.37	1.34	2.57	4.21	5.46	6.17	1.38	1.32	4.01	.582
11	-	-	-	-	-	-	-	-	-	-	-	-	-	-	-	-	.617
13	0.19	1.34	2.72	4.21	4.87	5.50	0.19	0.31	1.90	3.05	4.46	5.16	5.82	3.27	2.49	5.04	.653
15	0.19	1.13	2.04	3.16	3.65	4.37	0.19	0.21	1.51	2.57	3.98	4.60	5.50	5.49	4.69	7.55	.689
16	0.22	2.39	3.63	5.01	5.46	6.53	0.22	0.20	2.68	4.07	5.62	6.13	6.92	2.75	3.52	8.97	.759
18	0.19	5.99	7.67	8.91	9.72	12.3	0.22	0.47	5.99	8.12	9.99	11.6	13.8	1.74	2.49	5.34	.795
19	-	-	-	-	-	-	-	-	-	-	-	-	-	-	-	-	.812
20	0.19	7.55	8.12	8.91	9.72	11.0	0.19	0.47	7.99	9.65	11.9	13.7	13.8	.55	.83	5.04	.831
21	-	-	-	-	-	-	-	-	-	-	-	-	-	-	-	-	.848
22	0.26	19.0	1.62	13.3	13.7	11.0	0.21	2.35	16.0	7.67	15.8	14.5	9.78	.82	1.98	15.95	.866
23	-	-	-	-	-	-	-	-	-	-	-	-	-	-	-	-	.884
24	0.26	13.4	10.8	9.99	9.17	7.33	0.37	15.7	17.9	13.3	13.4	12.0	9.23	3.88	9.36	47.8	.902
25	0.31	7.12	8.12	9.44	7.72	6.17	0.49	23.5	10.1	11.2	11.2	8.66	6.92	6.91	32.9	25.28	.939
26	-	-	-				-	-	-	-	-			-		-	.976

TABLE VI

PEAK IN PRESSURE POWER SPECTRAL DENSITIES, Hz

α \ β	60°	40°	35°	30°	20°
0°	1400	1250	(b)	(b)	(c)
10°	1250	2000	(c)	(b)	(c)
20°	2100	1250	1300-1500	1500	(c)
25°	(a)	1400	1500	1700	(b)
30°	(a)	1400, 1450	1550	1800	(c)
33°	(a)	1300-1400	1500	1600	(b)
37°	(a)	1100	1450-1500	1600	(c)
Flap natural frequency	800	1150	1250	1200	2050

[a] Not run

[b] Not analyzed

[c] Broad spectrum

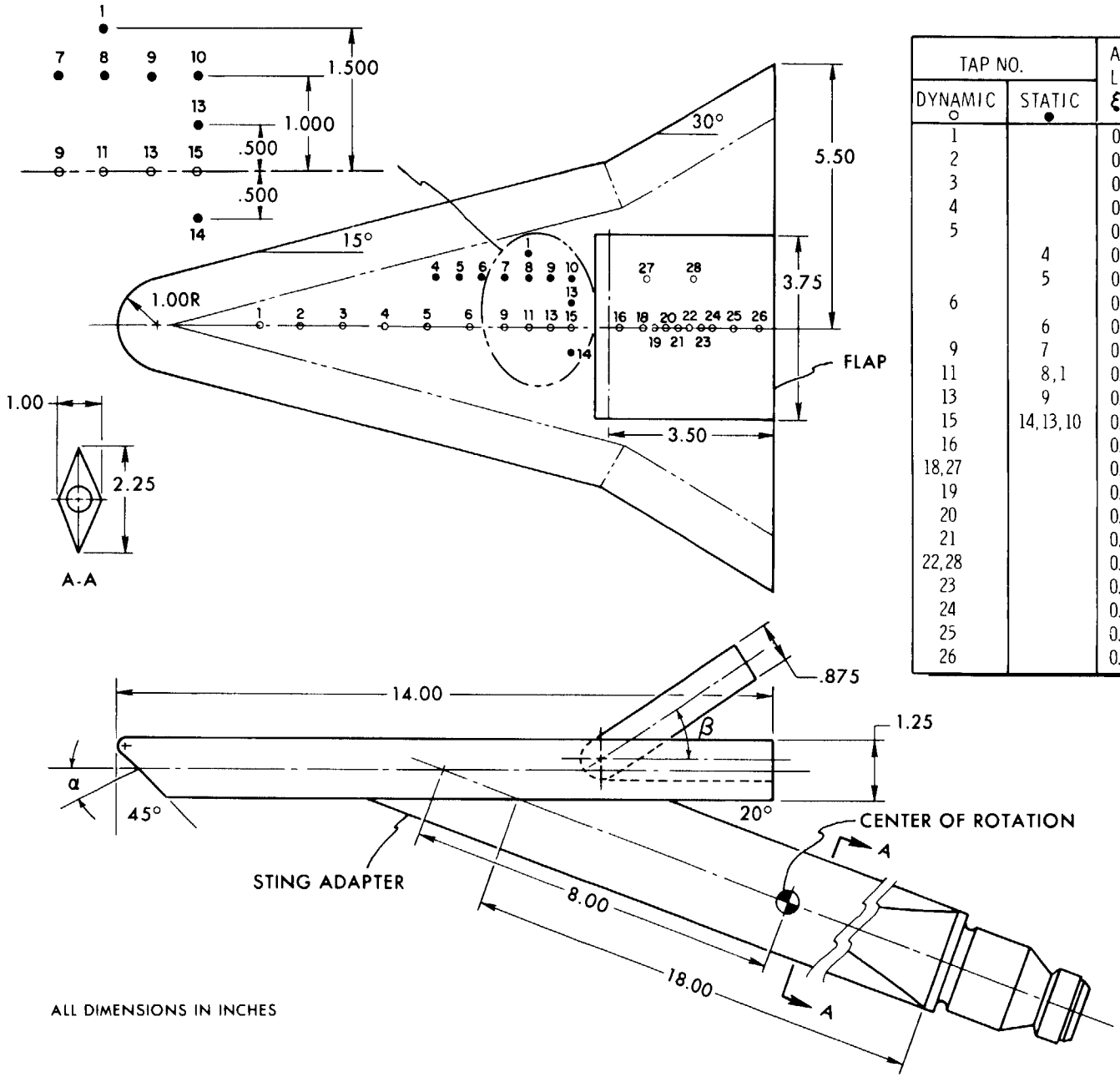

TAP NO.		AXIAL LOCATION
DYNAMIC ○	STATIC ●	$\xi = X/L$
1		0.210
2		0.274
3		0.337
4		0.401
5		0.465
	4	0.475
	5	0.510
6		0.528
	6	0.545
9	7	0.582
11	8, 1	0.617
13	9	0.653
15	14, 13, 10	0.689
16		0.759
18, 27		0.795
19		0.812
20		0.831
21		0.848
22, 28		0.866
23		0.884
24		0.902
25		0.939
26		0.976

Figure 2. - Details of model showing locations of instrumentation.

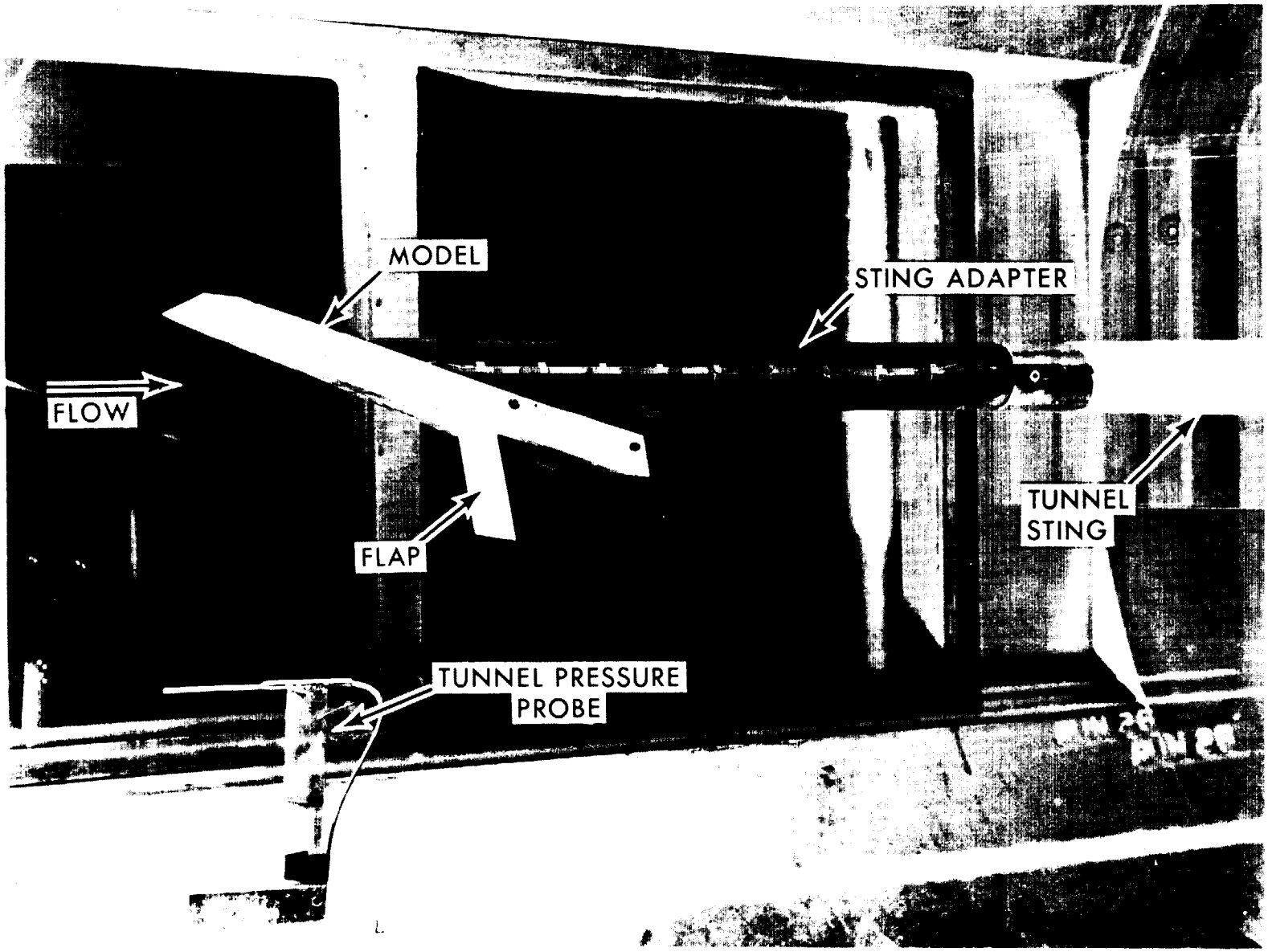

Figure 3. - Photograph of model in wind tunnel.

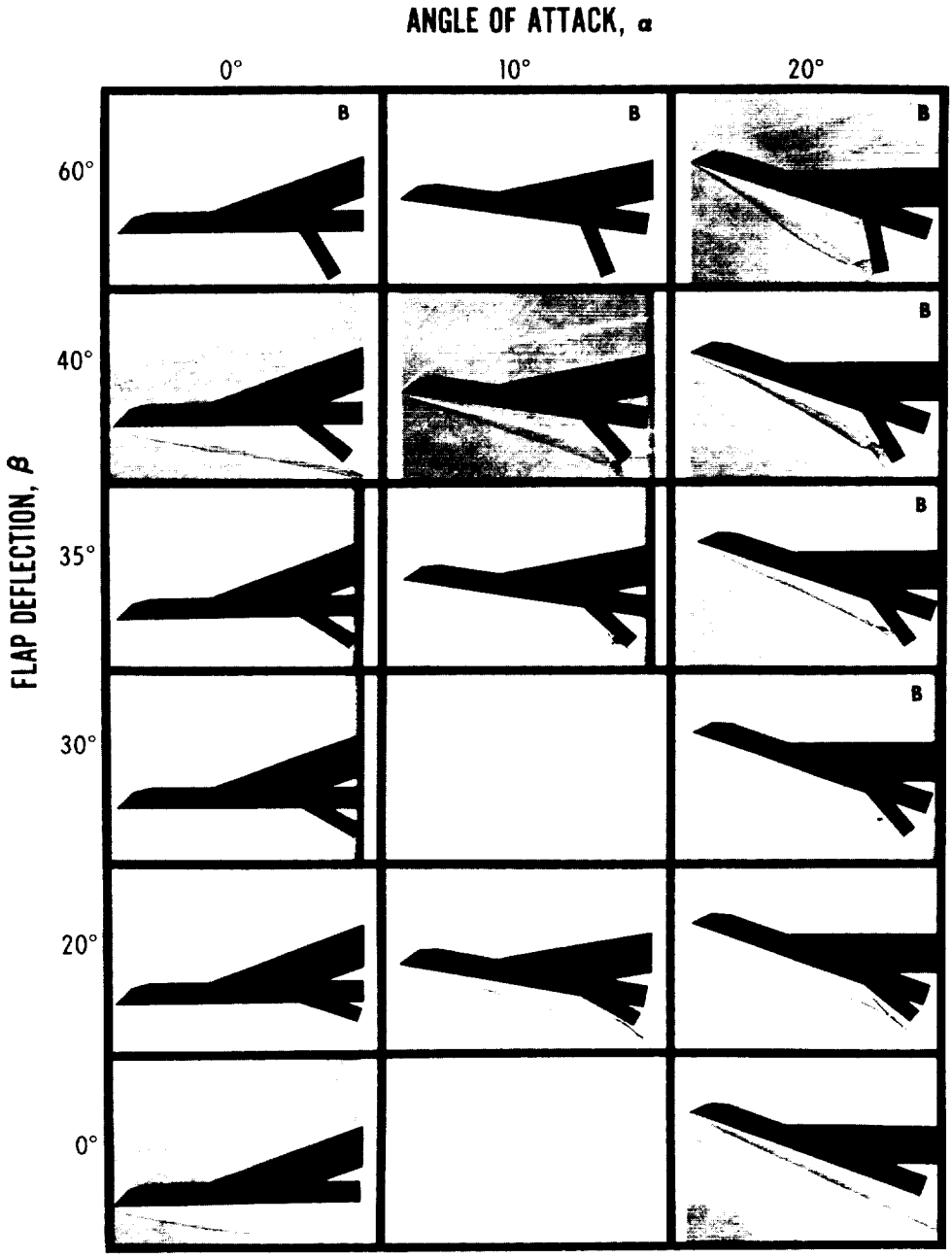

(a) α = 0° to 20°

Figure 4. - Mosaic of schlieren photographs.

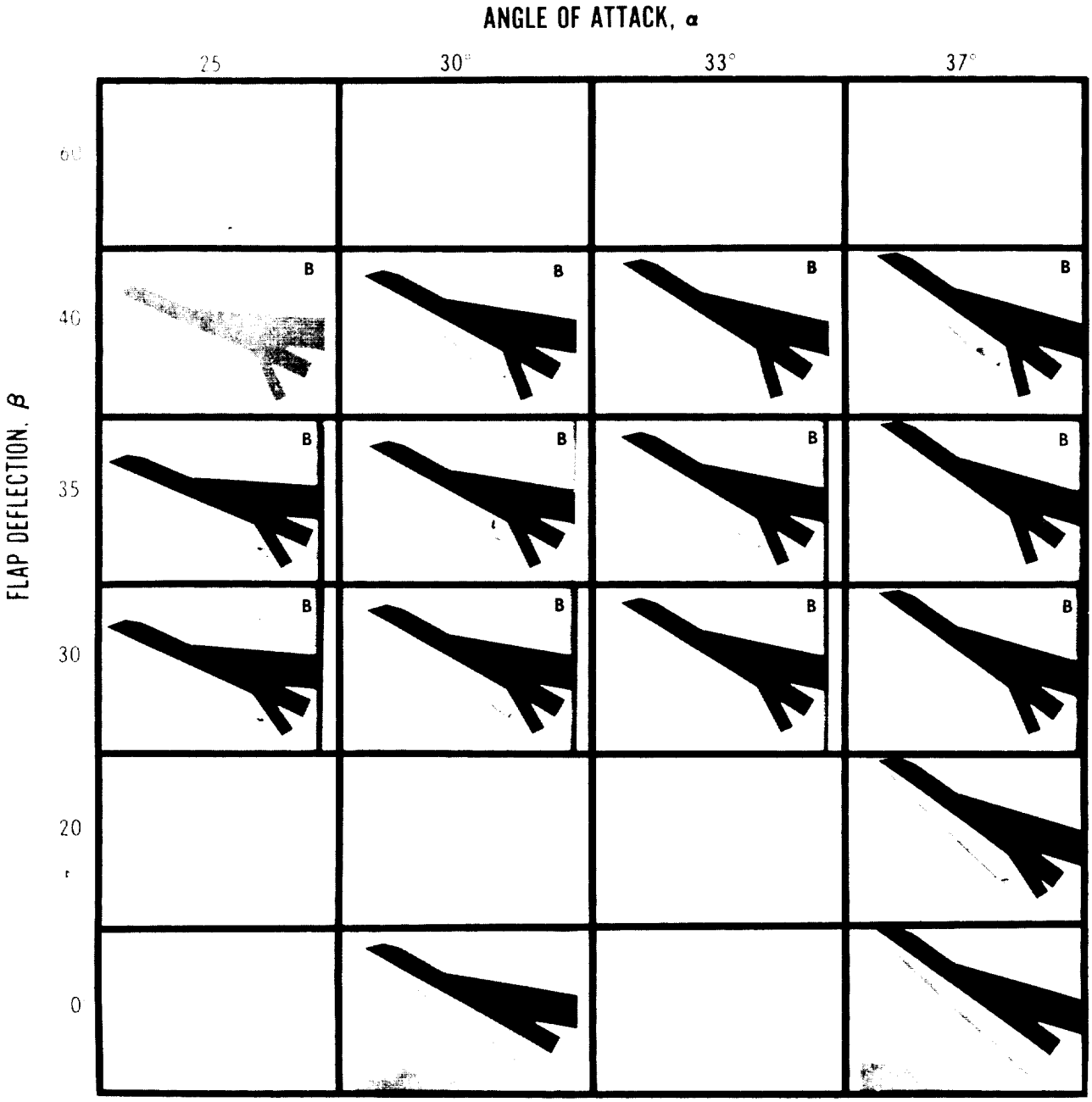

(b) α = 25° to 37°

Figure 4. - Concluded.

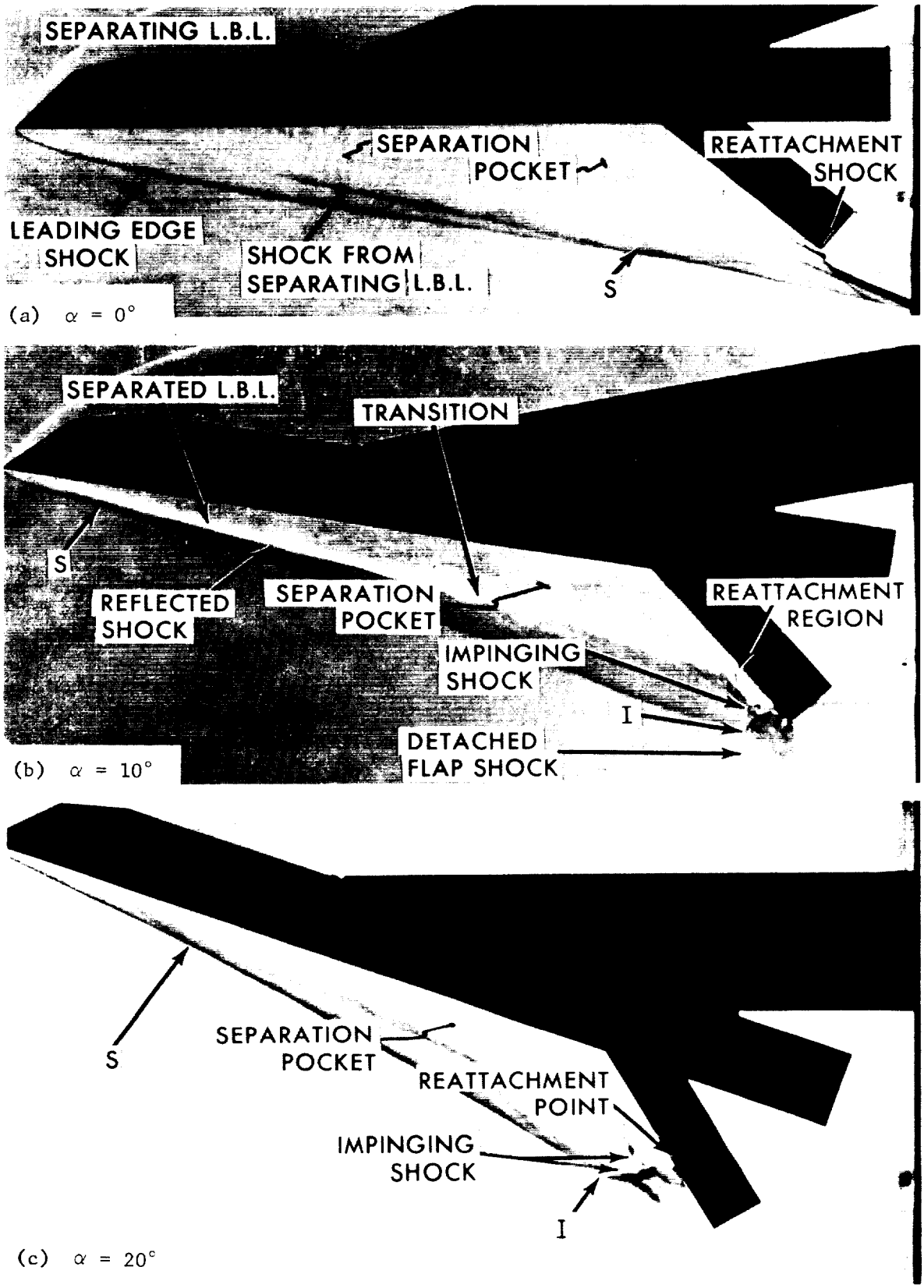

Figure 5. - Sequence of schlieren photographs for $\beta = 40°$.

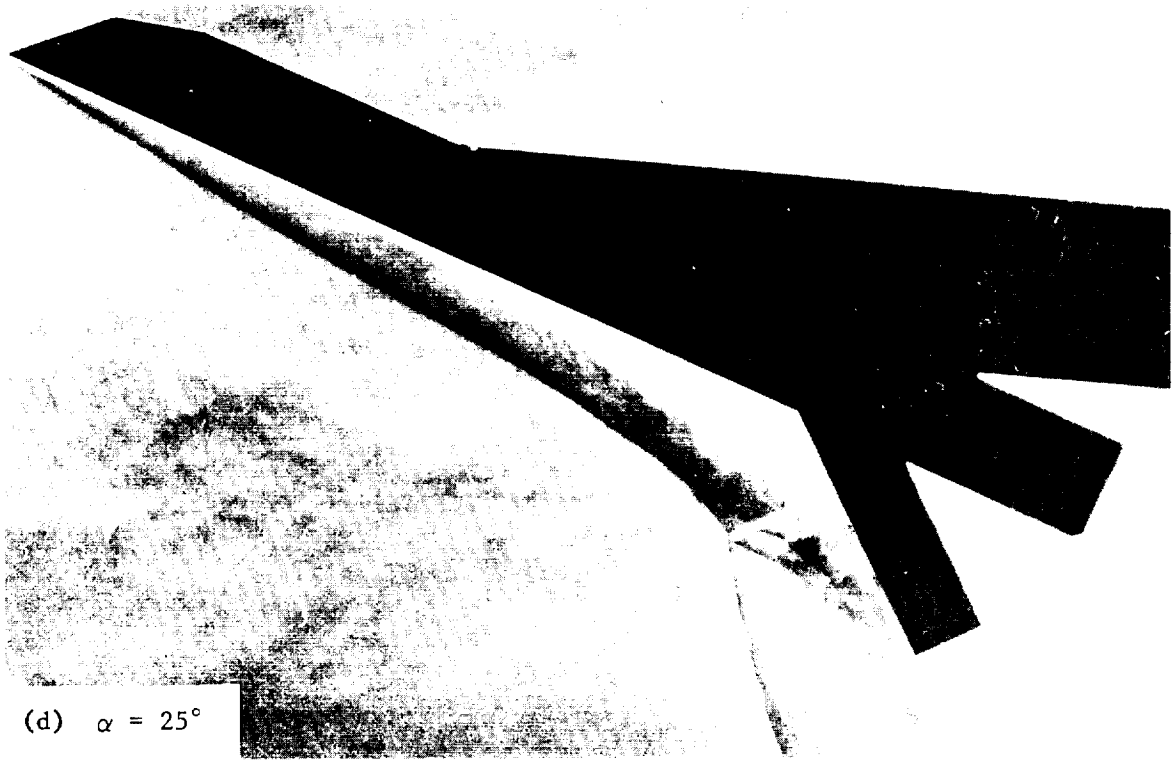

(d) $\alpha = 25°$

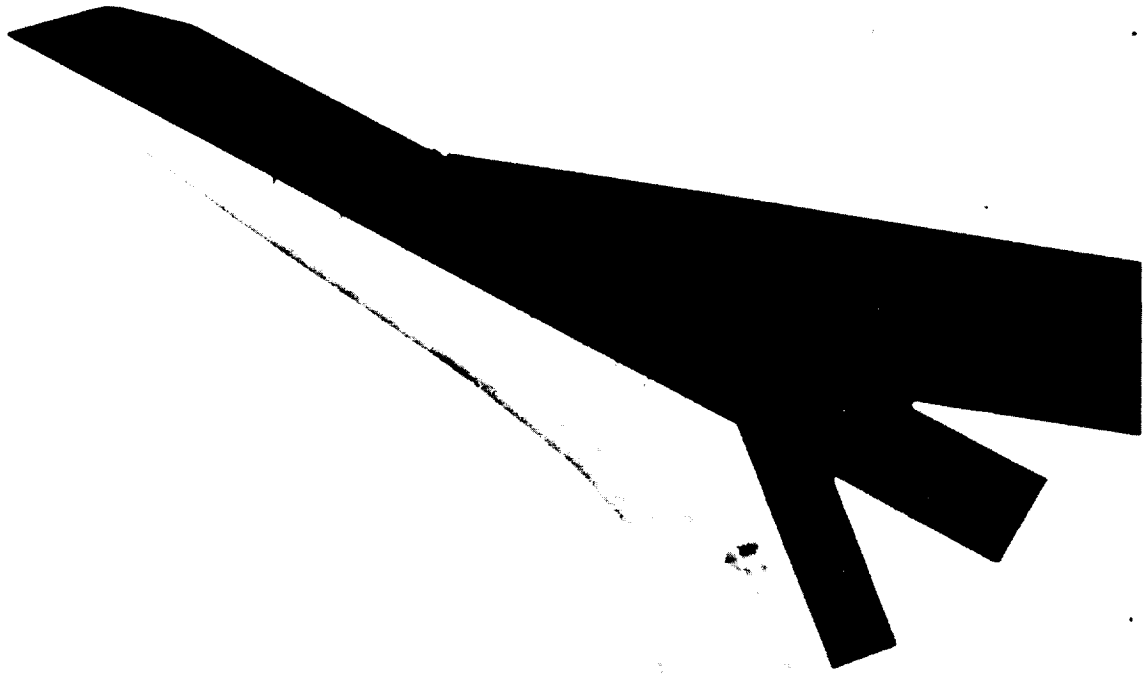

(e) $\alpha = 30°$

Figure 5. - Continued.

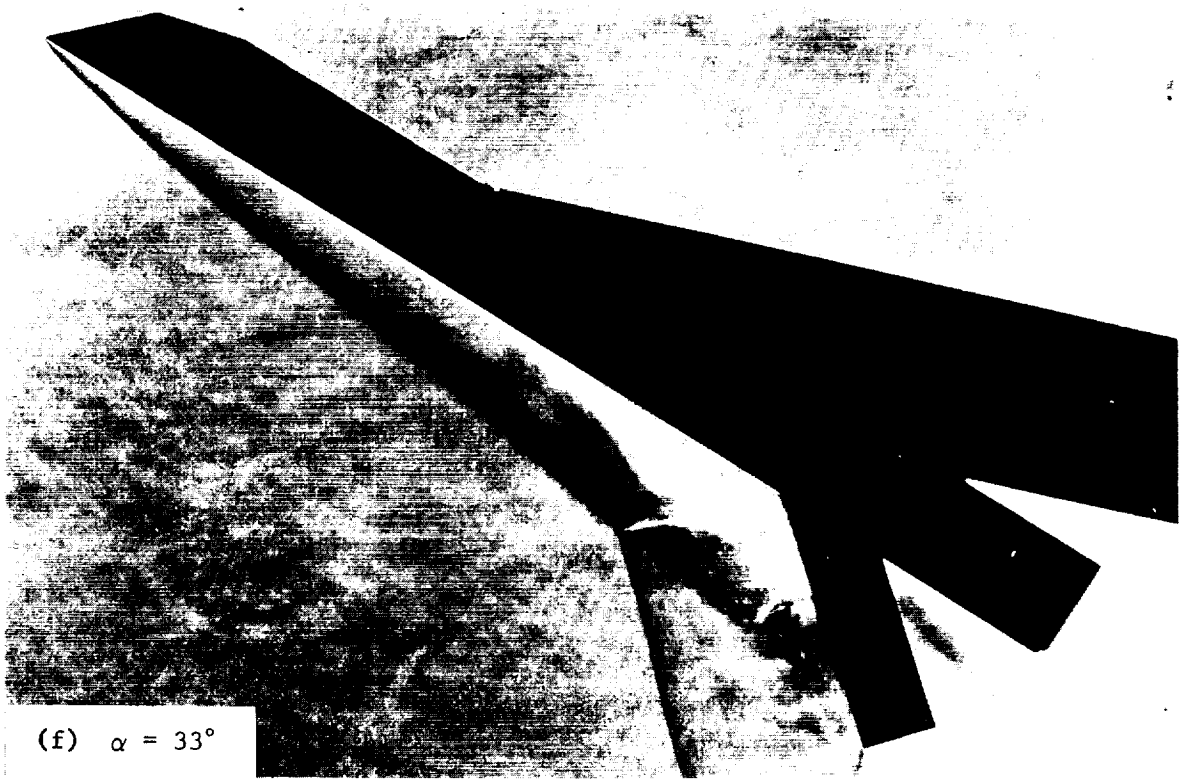

(f) $\alpha = 33°$

(g) $\alpha = 37°$

Figure 5. - Concluded.

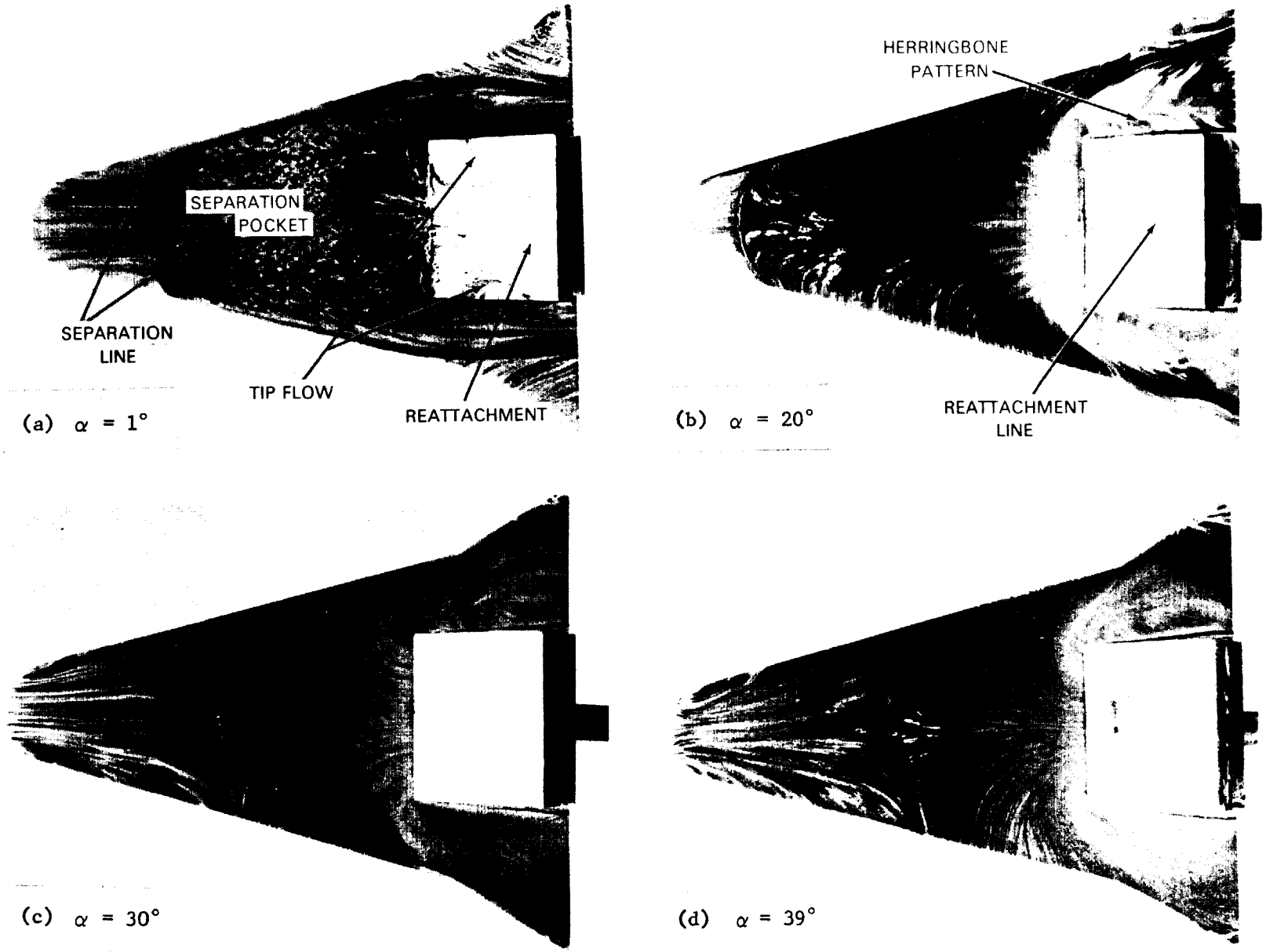

Figure 6. - Oil flow photographs.

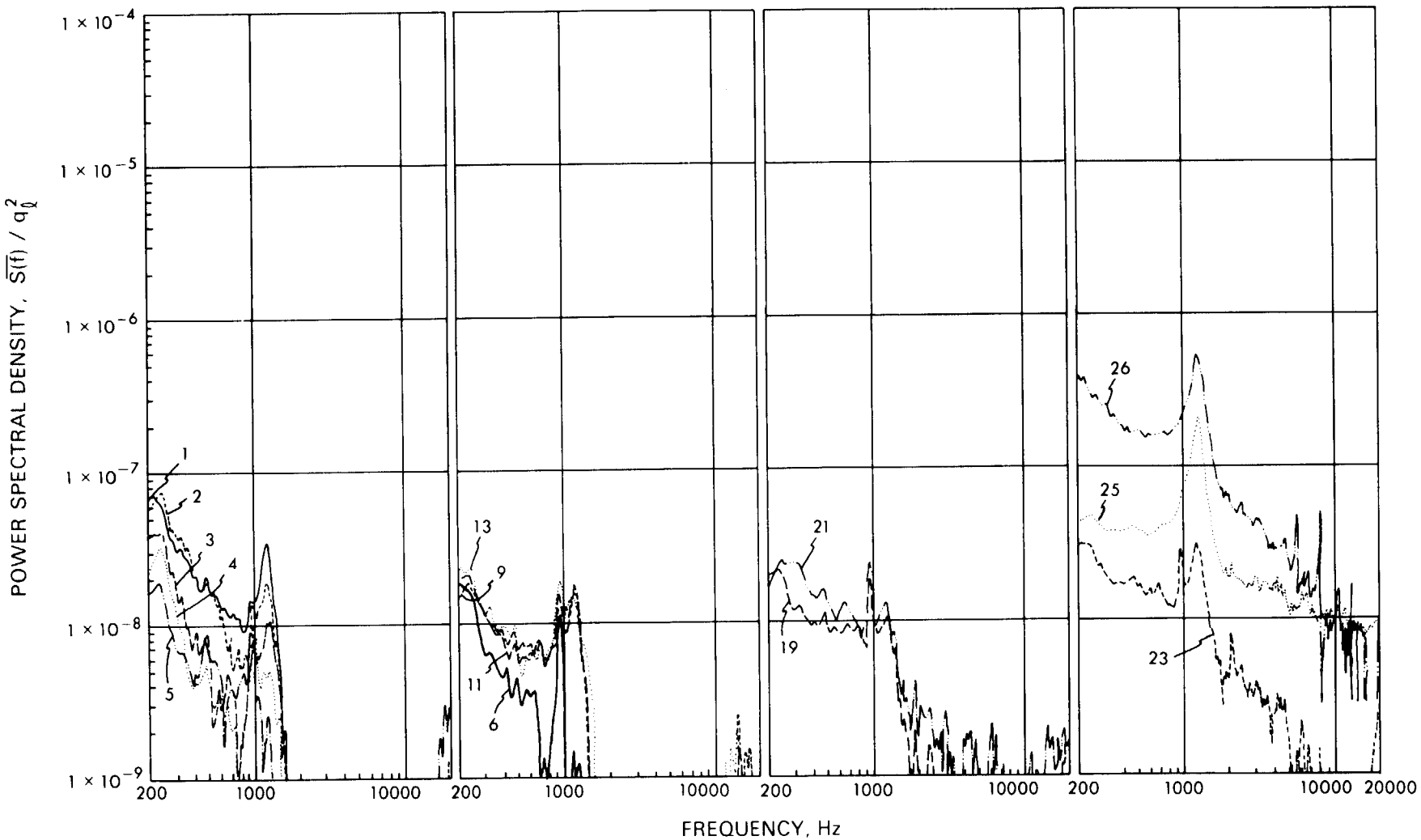

Figure 7. - Pressure power spectral densities, $\beta = 40°$, $\alpha = 0°$.

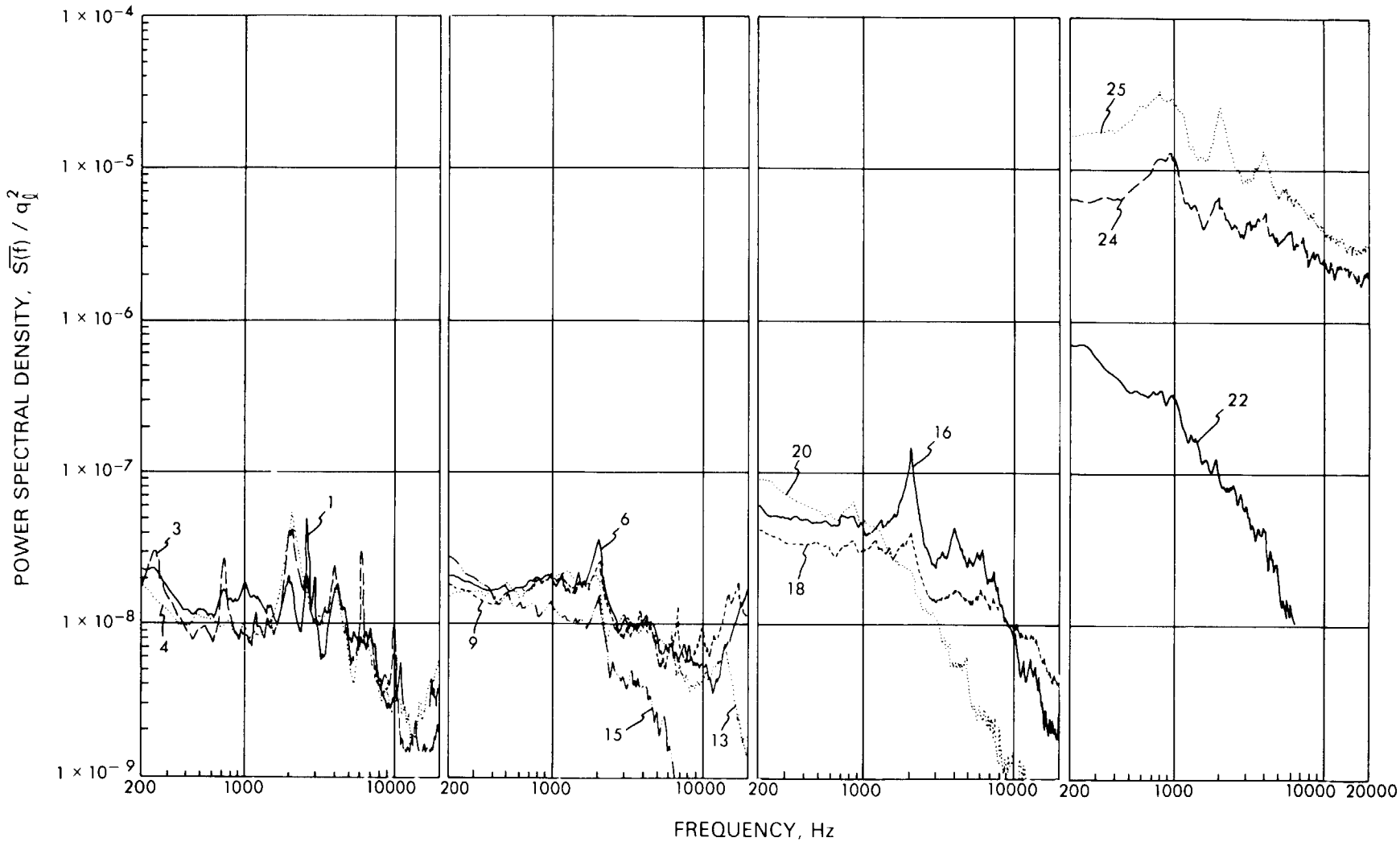

Figure 8. - Pressure power spectral densities, $\beta = 40°$, $\alpha = 10°$.

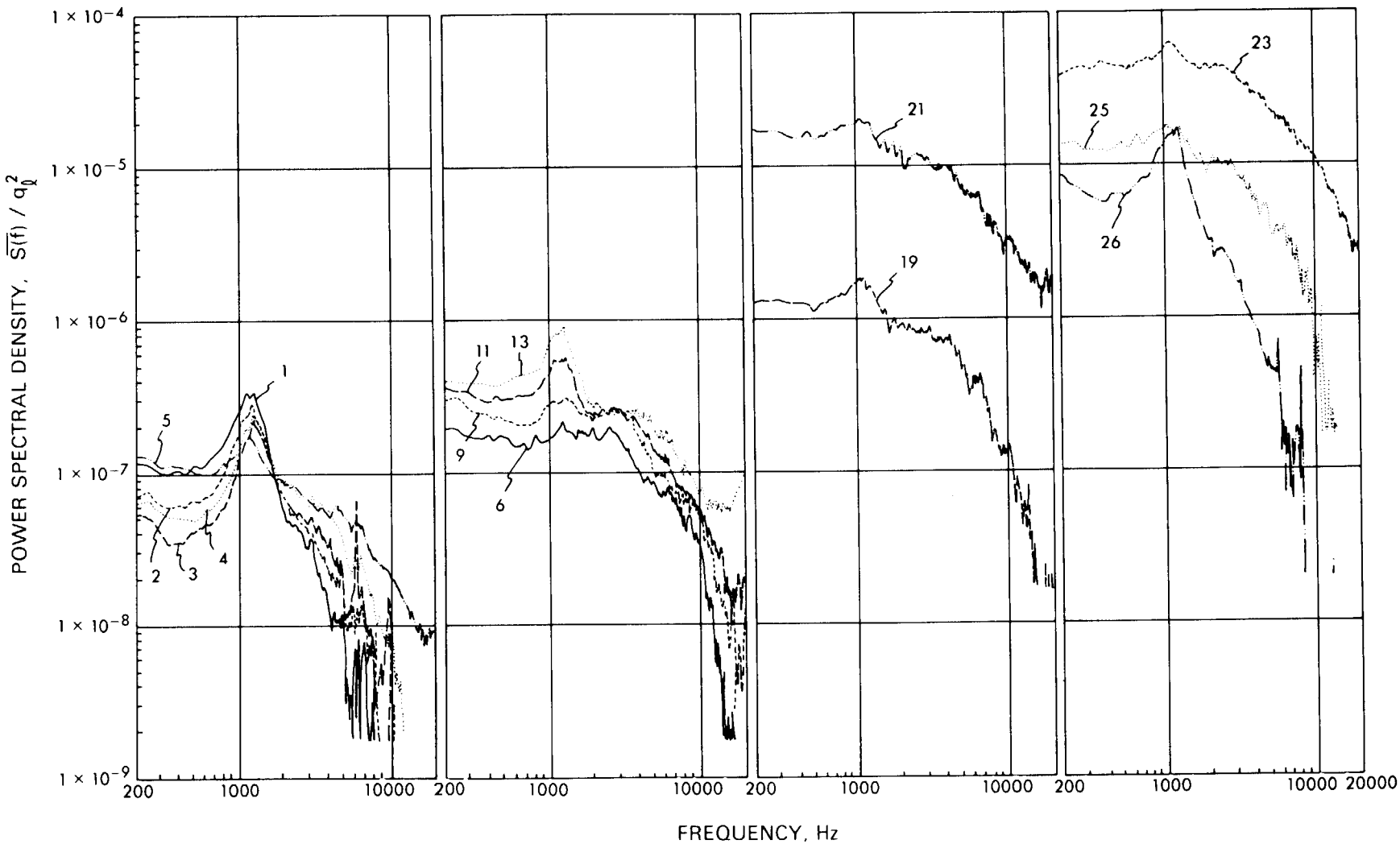

Figure 9. - Pressure power spectral densities, $\beta = 40°$, $\alpha = 20°$.

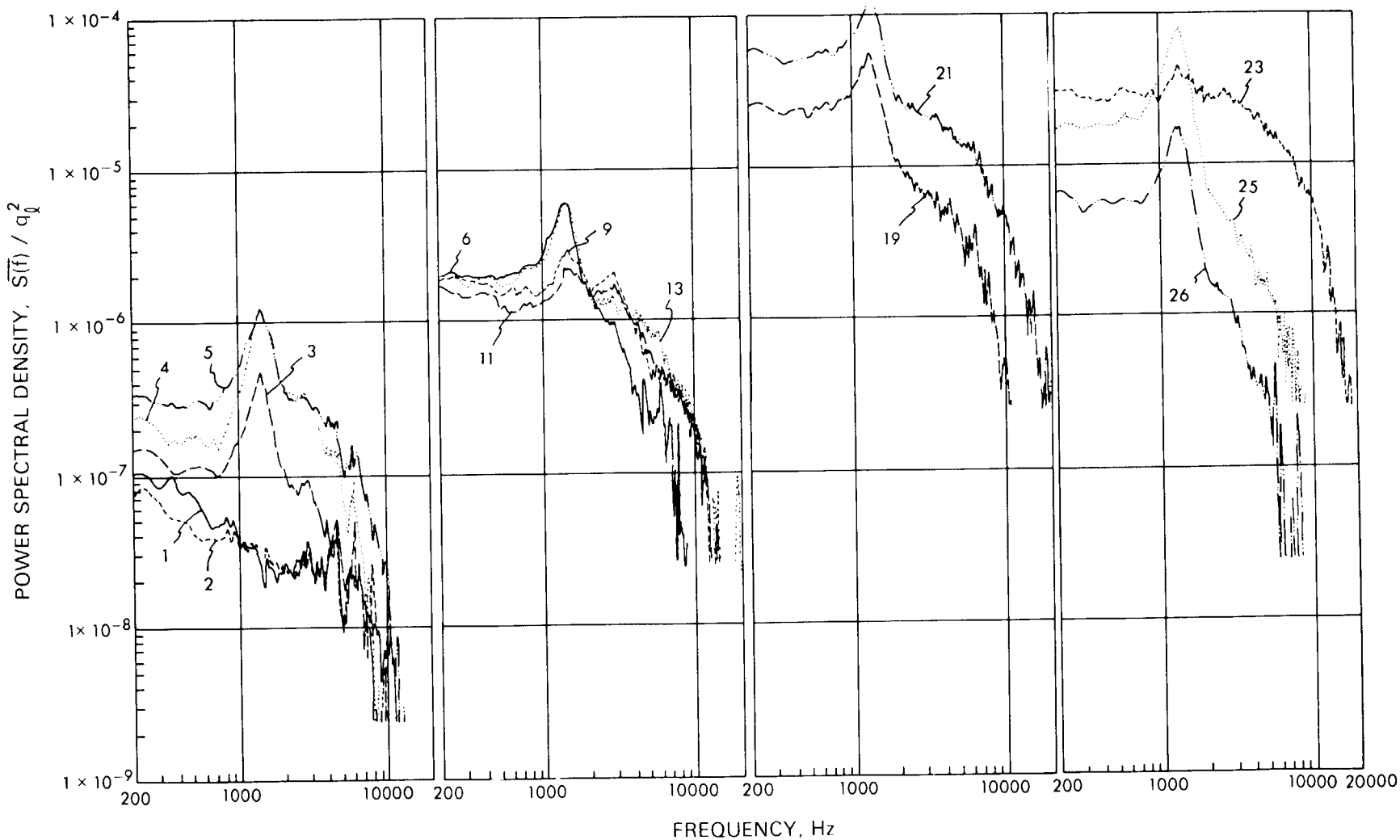

Figure 10. - Pressure power spectral densities, $\beta = 40°$, $\alpha = 30°$.

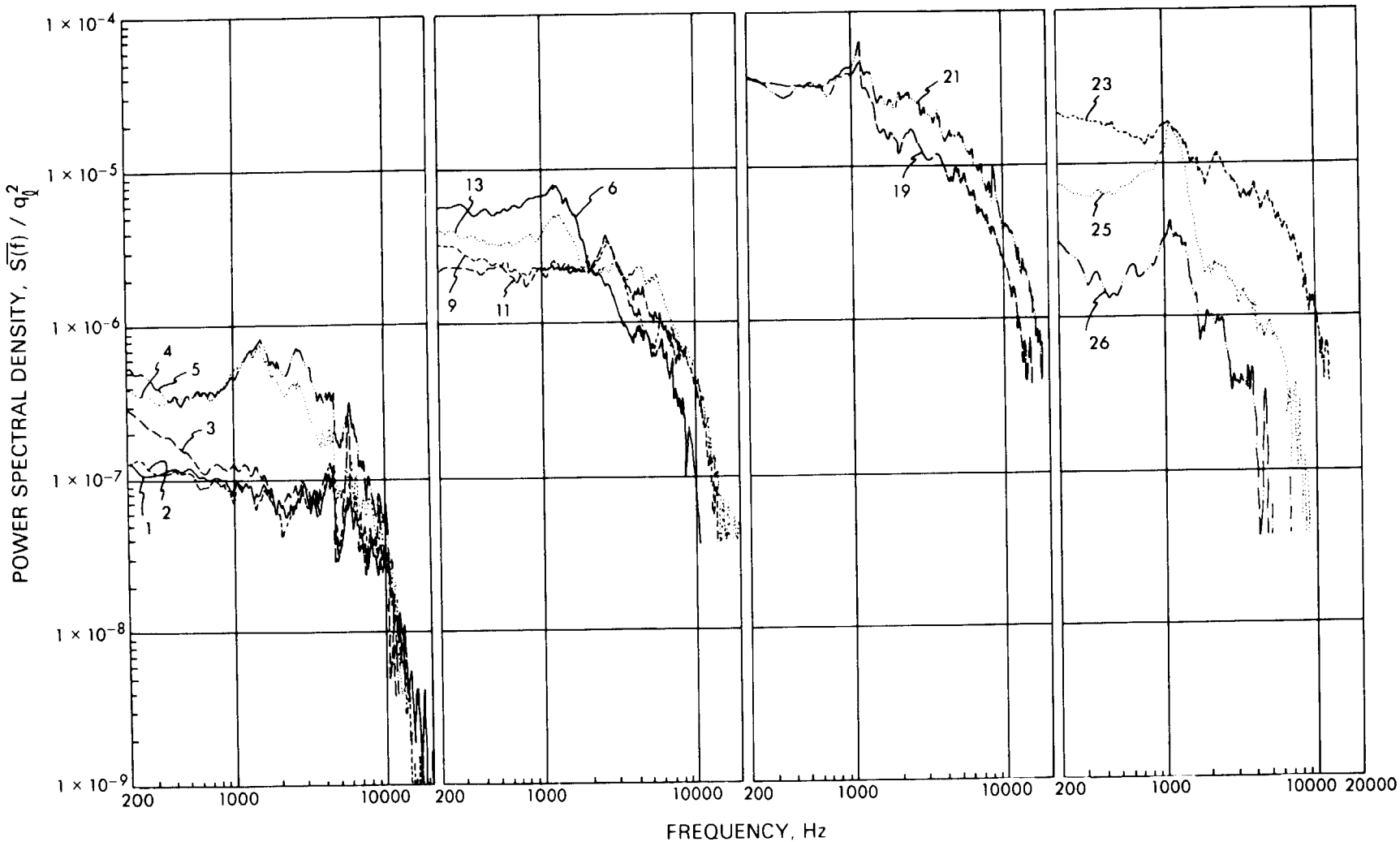

Figure 11. - Pressure power spectral densities, $\beta = 40°$, $\alpha = 37°$.

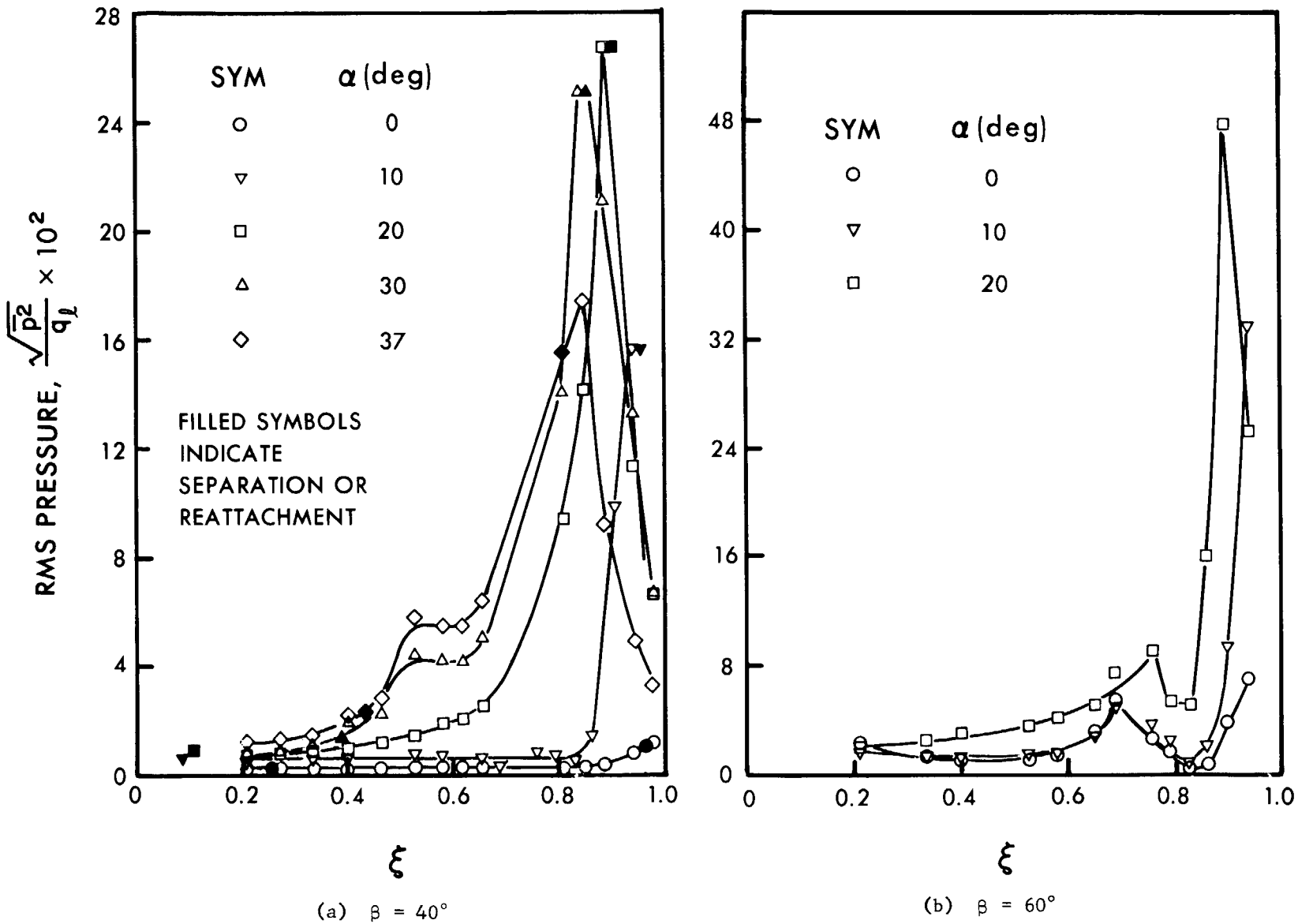

Figure 12. - Root mean squared pressure distribution.

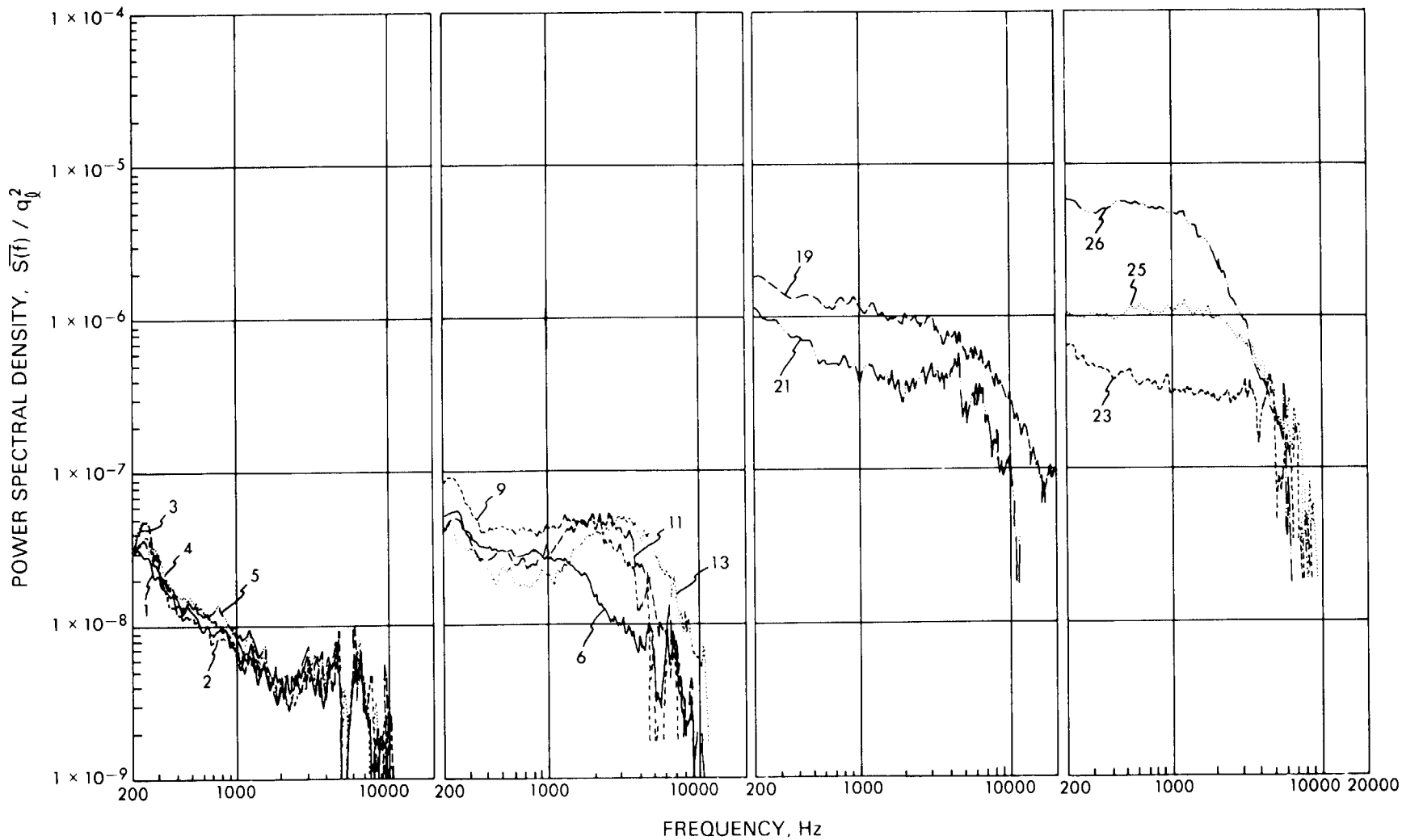

Figure 13. - Pressure power spectral densities, $\beta = 20°$, $\alpha = 20°$.

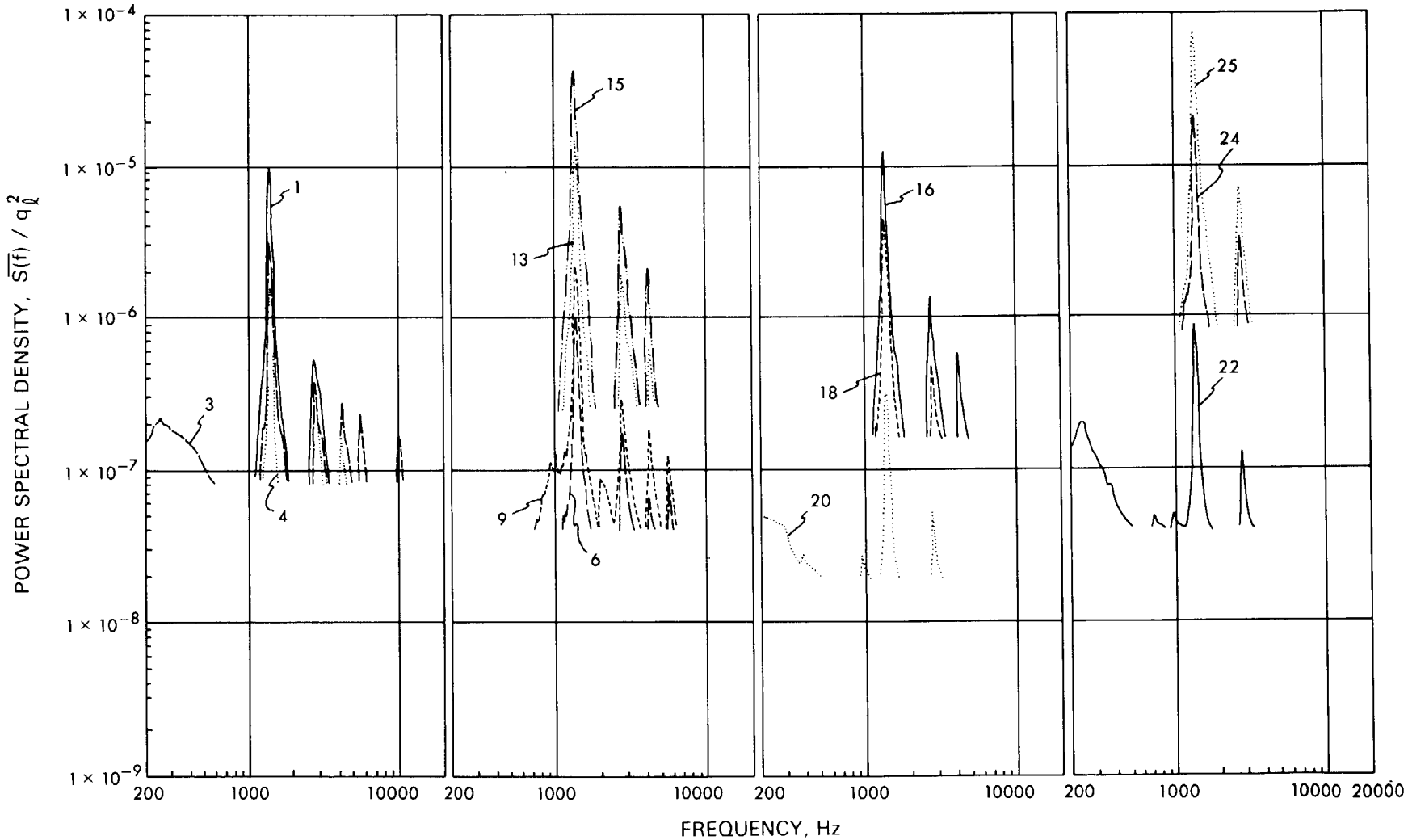

Figure 14. - Pressure power spectral densities, $\beta = 60°$, $\alpha = 0°$.

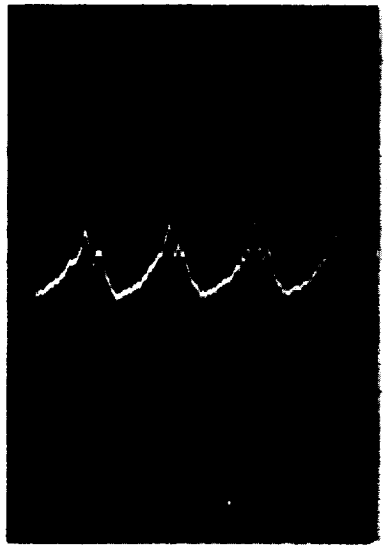

(a)

ξ = 0.210; 151-1/2 db SPL

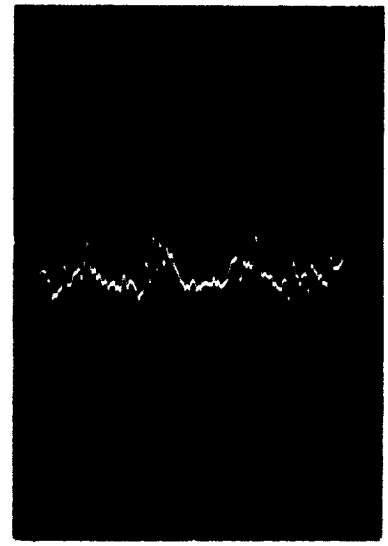

(b)

ξ = 0.528; 144-1/2 db SPL

(c)

ξ = 0.582; 147 db SPL

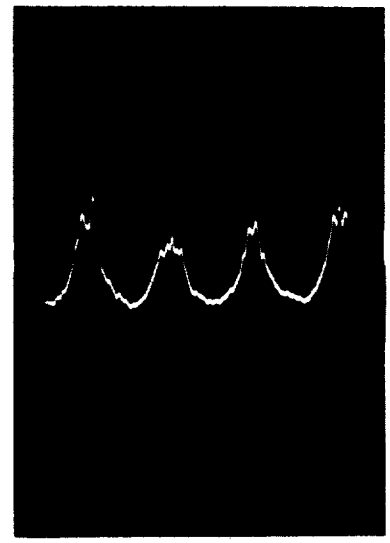

(d)

ξ = 0.939; 161 db SPL

Figure 15. - Pressure sensor scope traces, $\beta = 60°$.

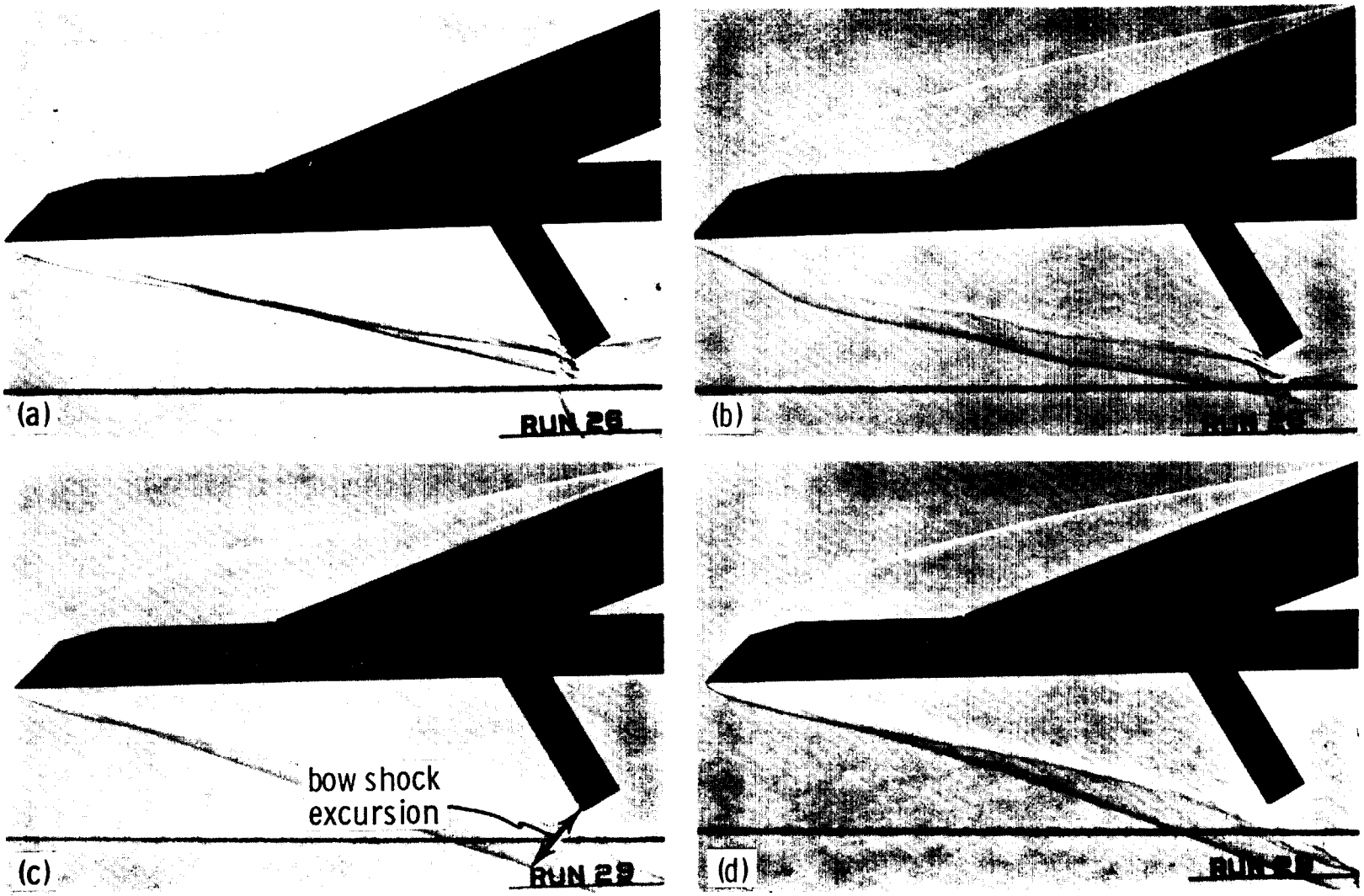

Figure 16. - Set of schlieren photographs for $\beta = 60°$, $\alpha = 0°$.